KINETIC ANALYSIS OF MHD BALLOONING MODES IN TOKAMAKS

By

W.M. Tang, G. Rewoldt, C.Z. Cheng, and M.S. Chance

OCTOBER 1984

PLASMA PHYSICS LABORATORY

PRINCETON UNIVERSITY
PRINCETON, NEW JERSEY

PREPARED FOR THE U.S. DEPARTMENT OF ENERGY,
UNDER CONTRACT DE-AC02-76-CHO-3073.

KINETIC ANALYSIS OF MHD BALLOONING MODES IN TOKAMAKS

W. M. Tang, G. Rewoldt, C. Z. Cheng, and M. S. Chance

Plasma Physics Laboratory, Princeton University

P.O. Box 451

Princeton, New Jersey 08544

PPPL--2155

DE85 002707

ABSTRACT

A comprehensive analysis of the stability properties of the appropriate kinetically generalized form of MHD ballooning modes together with the usual trapped-particle drift modes is presented. The calculations are fully electromagnetic and include the complete dynamics associated with compressional ion acoustic waves. Trapped-particle effects along with all forms of collisionless dissipation are taken into account without approximations. The influence of collisions is estimated with a model Krook operator. Results from the application of this analysis to realistic tokamak operating conditions indicate that unstable short-wavelength modes with significant growth rates can extend from $\beta = 0$ to values above the upper ideal-MHD-critical-beta associated with the so-called second stability regime. Since the strength of the relevant modes appears to vary gradually with β, these results support a "soft" beta limit picture involving a continuous (rather than abrupt or "hard") modification of anomalous transport already present in low-β-tokamaks. However, at higher beta the increasing dominance of the electromagnetic component of the perturbations indicated by these calculations could also imply significantly different transport scaling properties.

1. INTRODUCTION

Estimates of beta (ratio of plasma to magnetic pressure) limits in toroidal systems have continued to be based in large part on the stability properties of ideal magnetohydrodynamic (MHD) ballooning modes. It has been established in previous work that kinetic modifications can be important for these fine-scale (short-wavelength) instabilities [1-7]. In particular, when finite gyroradius effects associated with ion diamagnetic drifts are taken into account together with radial modifications ("finite-n corrections") to the leading order local theory, it is found that significantly more optimistic critical beta (β_c) values can result for specific tokamak equilibria of interest [7]. On the other hand, in the long mean-free-path limit, collisionless dissipation in the form of magnetic drift resonances can generate residual shear-Alfvén microinstabilities [3-5]. In general, a realistic assessment of the importance of this class of instabilities requires a comprehensive kinetic treatment.

The analysis described in this paper is fully electromagnetic and includes the dynamics associated with the compressional ion acoustic waves. In the long mean-free-path limit, trapped-particle effects together with all forms of collisionless dissipation (bounce, transit, and magnetic drift frequency resonances) are taken into account without approximations. For shorter mean-free-path regimes, the influence of collisional dissipation is estimated by employing a model Krook operator. A stability code, which incorporates the numerous effects just described, was previously developed to study electromagnetic modifications of electrostatic trapped-particle drift modes [8]. In the present investigation this code is used to analyze the kinetically generalized form of the MHD ballooning modes (associated with shear-Alfvén waves) together with the usual trapped-particle modes (associated

with drift waves). By properly determining the relative strength of the dominant instabilities (as indicated by their growth rates), the significance of ideal MHD ballooning mode beta limits can be more meaningfully assessed.

The main qualitative features of the analysis are discussed in Sec. 2. In particular, it is demonstrated that even in the ideal MHD limit, the compressional coupling to acoustic waves can significantly modify the growth rates. Results from the application of the comprehensive kinetic stability code to both model and numerical MHD equilibria for parameters appropriate to a number of existing tokamaks are presented in Sec. 3. Also included in this section are comparisons of these results with those from ideal MHD (without acoustic effects) and simplified kinetic model calculations. Typical trends indicated by these studies are briefly summarized and their implications discussed in Sec. 4.

2. STABILITY ANALYSIS

Previous kinetic studies have indicated that the presence of short-wavelength instabilities in tokamaks is very likely to be unavoidable [8]. Viewed in this context, the significance of critical beta values for ballooning modes becomes tied to their strength relative to other instabilities when β_c criteria are violated. Hence, instead of considering threshold conditions, the more relevant problem involves the proper evaluation of the growth rates for the dominant modes. By making use of the ballooning representation, the principal linear properties of these large toroidal mode number ($n \gg 1$) instabilities can be accurately determined with a one-dimensional (along the magnetic field line) calculation which is radially local on each magnetic flux surface.

2.1 Ideal MHD With Compressional Acoustic Effects

As shown in Ref. 9, the ideal MHD ballooning modes are governed by two coupled ordinary differential equations of the form

$$\underline{B} \cdot \nabla\left(\frac{|\underline{k}_\perp|^2}{B^2}\,\underline{B} \cdot \nabla\right)\phi + \frac{\omega^2}{v_A^2}\,|\underline{k}_\perp|^2\,\phi + 2\kappa_w\left[(\nabla P \times \underline{B} \cdot \underline{k}_\perp)\,\frac{\phi}{B^2}\right.$$

$$\left. + \Lambda B^2\left(\underline{B} \cdot \nabla \xi_B - 2\kappa_w \phi\right)\right] = 0 \qquad (1)$$

and

$$\underline{B} \cdot \nabla\left[\Lambda B^2\left(\underline{B} \cdot \nabla \xi_B - 2\kappa_w \phi\right)\right] + \frac{\omega^2}{v_A^2} B^4 \xi_B = 0 \qquad (2)$$

where $\Lambda \equiv \gamma P/(B^2 + \gamma P)$, $\kappa_w \equiv (\hat{n} \cdot \nabla \hat{n}) \times (\underline{B} \cdot \underline{k}_\perp / B^2)$, $\hat{n} \equiv (1/B)\underline{B}$, γ is the ratio of specific heats, v_A is the Alfvén speed, $\underline{k}_\perp$ is the spatially dependent perpendicular wave vector, ϕ is the stream function for the cross-field displacement, and ξ_B is the displacement along the field line. In general, Eqs. (1) and (2) can be combined to give a fourth order differential eigenmode equation. However, if compressional acoustic effects are ignored, then Eq. (2) and the last term in Eq. (1) can be dropped, and the familiar second-order differential equation for ballooning modes is recovered [10,11].

Although it is well known that the compressional acoustic effects do not modify β_c, it is nevertheless important to take them into account when calculating ballooning mode growth rates. This can be illustrated by considering the simple local limit of Eqs. (1) and (2). Specifically, taking $k_\perp \to k_\perp$ and $\hat{n} \cdot \nabla \to ik_\parallel$, Eqs. (1) and (2) are easily combined to give an algebraic eigenvalue equation of the form

$$\Omega^2 - 1 + D - \frac{\delta\Lambda\Omega^2}{\Omega^2-\Lambda} = 0 \tag{3}$$

where $\Omega \equiv \omega/\omega_A$, $\omega_A \equiv k_\parallel v_A$, $D \equiv \beta/L_p L_\kappa k_\parallel^2$, $\beta \equiv 2p/B^2$, $\delta \equiv 4/k_\parallel^2 L_\kappa^2$, and L_p and L_κ represent the pressure gradient and magnetic curvature scale lengths with $|\nabla p/p| \to 1/L_p$ and $|\kappa_w| \to (k_\perp/B)(1/L_\kappa)$. The solution is just

$$\Omega^2 = \frac{1}{2}\left\{1 - D + \bar{\Lambda} \pm \left[(1 - D + \bar{\Lambda})^2 - 4\Lambda(1-D)\right]^{1/2}\right\} \tag{4}$$

with $\bar{\Lambda} \equiv \Lambda(1 + \delta)$. If acoustic effects are ignored, the usual estimate for the ballooning mode eigenvalue is simply

$$\Omega^2 = 1 - D \tag{5}$$

with the marginal stability boundary at $D = 1$ or, equivalently, at $\beta = \beta_{crit} = L_p/Rq^2$ for $k_\parallel = 1/qR$ and $L_\kappa = R$.

As is evident from Eq. (4), the instability threshold for ballooning modes given by Eq. (5) is unchanged by acoustic modifications. On the other hand, it is also clear that if the modes become unstable (i.e., for $D > 1$), the magnitude of the resultant growth rates can be significantly decreased by such effects. For example, if $D = 1 + \delta$, then Eq. (5) overestimates the unstable eigenvalue $(-\Omega^2)$ by a factor of $(1 + \delta)^{1/2}$ compared to the appropriate result (including acoustic effects) from Eq. (4).

The trend toward smaller growth rates indicated by the simple local estimates is confirmed by actual numerical solutions to both the usual second order differential ballooning mode equation and to the fourth order form which includes the acoustic effects. These calculations have been applied to realistic (numerical) MHD equilibria with typical results displayed in

Fig. 1. Here the unstable eigenvalue ($-\Omega^2$) is plotted as a function of the radial coordinate (ψ/ψ_{TOT}) with ψ being the poloidal flux function. Note that the fourth order equation gives the same result as the second order equation at the marginally stable surface ($-\Omega^2 = 0$ at $\psi/\psi_{TOT} = 0.14$) but yields considerably smaller growth rates on the unstable surfaces.

2.2 Kinetic Effects on Ballooning Modes

The basic procedure required for a comprehensive analysis of the influence of kinetic effects on ballooning modes has been presented in detail in Refs. 1 and 8. Using the most general form of the perturbed distribution function (derived from the gyrokinetic equation) together with the quasineutrality condition and the parallel and perpendicular components of Ampere's law leads to a complicated set of three coupled integro-differential equations [8] which must be solved numerically. Complete trapped-particle dynamics are included in these equations which are valid for arbitrary mode frequency compared to the particle bounce or transit frequency and also for arbitrary perpendicular wavelength compared to the particle gyroradius or banana width. Hence, all forms of collisionless dissipation in the form of bounce, transit, and magnetic drift frequency resonances as well as the compressional acoustic effects noted in Sec. 2.1 are included here without approximations.

In the shorter mean-free-path regimes where collisional dissipation is important, an energy and pitch-angle-dependent Krook operator is used to model such effects. When applied to electrostatic instabilities in the banana regime, this model collision operator can reproduce the results of a Lorentz operator in the limits $|\omega| << \nu_{eff}$ and $|\omega| >> \nu_{eff}$ with ν_{eff} being the effective collision frequency and ω being the mode frequency [12]. However,

for the more general electromagnetic cases considered in the present investigation, the accuracy of the model operator remains to be established.

A detailed description of the final system of three coupled linear, homogeneous, non-Hermitian integro-differential equations and the numerical procedure used to solve them are given in Ref. 8. The Ritz method employed involves expanding the unknown eigenfunctions in terms of an appropriate set of basis functions. This generates a single large matrix equation which is solved by standard numerical techniques to give the eigenvalues and eigenfunctions of the system. The code developed to carry out these calculations has been interfaced with analytic model MHD equilibria as well as with general numerical MHD equilibria.

2.3 Partial Kinetic Model Calculations

Before presenting the results from the application of the comprehensive kinetic analysis to specific tokamak operating conditions, it should be pointed out that useful information has also been gained from simplified kinetic model calculations. At the simplest level, the kinetic eigenmode equations in the ideal MHD limit just reduce to Eqs. (1) and (2) [1]. If compressional coupling to the acoustic waves and trapped-particle effects are ignored, important kinetic modifications associated with finite ion gyroradius effects and magnetic drift frequency resonances can be studied with a second-order differential eigenmode equation [1, 3-5]. Trapped-electron effects, which introduce an integral equation character to the problem, have been modelled in this type of calculation by ignoring the orbit-averaged nature of the trapped-particle response [5]. In general, the reduced kinetic model approach can provide a much faster means of estimating the importance of specific physics effects and their associated analytic trends. However,

comparisons with representative results from the comprehensive kinetic code are of course necessary to determine the validity of the approximations invoked. To illustrate this point, both the full kinetic analysis and the reduced kinetic model of Ref. 5 have been applied to a relevant set of tokamak cases in Sec. 3.

3. RESULTS

In this section the results from the application of the stability analysis (described in Sec. 2) to operating conditions characteristic of a number of existing tokamaks are presented. As noted earlier, the dominant type of short-wavelength instabilities at low β is the trapped-electron drift mode [8], and the dominant type at high β is the kinetic-ballooning mode (associated with shear-Alfvén waves) [1-7]. The calculations here deal with both classes of instabilities and address the important issues concerning: (a) the relative strength of the dominant modes as a function of beta; (b) the accuracy of ideal MHD and reduced kinetic model estimates of growth rates; (c) the influence of collisional dissipation; and (d) characteristic eigenfunctions and typical wave number spectra.

Previous studies have demonstrated that the linear properties of short-wavelength toroidal instabilities are well represented by the leading order (radially local) solutions to the ballooning formalism hierarchy of equations [13]. In the present analysis, the complete kinetic form of the one-dimensional (along the magnetic field line) eigenmode equations are solved on a representative magnetic surface (where the much simpler ideal MHD and reduced kineti. calculations indicate the relevant modes to be the strongest). The fastest growing instabilities tend to be those which are localized around the magnetic field minimum at the outside of the torus and to

be characterized by perturbed potentials with the least number of nodes [8]. For such modes the appropriate choice for the local ballooning parameter θ_o [13] is zero. When this parameter is varied, specific calculations of the eigenvalue (ω) confirm that $\theta_o = 0$ is an extremum in ω for up-down symmetric equilibria. That this choice is in fact found to maximize the growth rate is also an expected result, since the destabilizing effects associated with trapped particles and unfavorable curvature are known to be the strongest at the outside of the torus. Additional modifications from the influence of impurities [14], energetic particles with non-Maxwellian equilibrium distribution functions [15], and equilibrium electric fields [16] will not be treated here.

With regard to the specific tokamak experiments considered, input parameters in the calculations were chosen to be representative of conditions in: (a) ISX-B (Impurity Study Experiment); (b) PDX (Poloidal Divertor Experiment) during its normal mode of operation ("L-mode") and during its improved confinement mode of operation ("H-mode"); and (c) Doublet-III. Although realistic numerical equilibria from MHD codes [17] can be employed in this type of analysis [8], it is far more convenient to use an analytic model equilibrium [10,11] when investigating general β-dependent trends. This frequently used equilibrium [2-5] is characterized by circular magnetic surfaces, large aspect ratio, and the Shafranov shift modelled by a term proportional to the local pressure gradient. When dealing with problems where β remains fixed, the more realistic equilibria [17] can be readily employed. This procedure is in fact carried out in Sec. 3.2 where the relative strength of the instabilities in the "L-mode" and "H-mode" of operation in the PDX experiment are calculated.

3.1 ISX-B

In considering the ISX-B experiment [18], input parameters in the stability studies were chosen to be typical of neutral-beam-heated deuterium plasmas where β_o (beta at the magnetic axis) = 10% and $<\beta>$ (volume-averaged beta) = 3% [19]. On a representative magnetic surface (r/a = 0.35 with a being the plasma radius), the specific local parameters are: $\epsilon_o \equiv r/R_o = 0.10$, $T_e = 1.26$ keV, $T_i = 1.16$ keV, $q = 1.20$, $r\, d\, \ell n\, q/dr = 0.62$, $n_e = 6.57 \times 10^{13} cm^{-3}$, $\eta_e \equiv (d\, \ell n\, T_e/dr)/(d\, \ell n\, n_e/dr) = 1.09 = \eta_i$, n (toroidal mode number) = 5 and corresponding $k_\theta \rho_i = 0.15$ with $k_\theta = nq/r$ and ρ_i being the ion gyroradius, $\nu_e^* \equiv (\nu_{eff}/\bar{\omega}_b)_e = 0.145$ with ν_{eff} and $\bar{\omega}_b$ being the effective collision and average bounce frequencies, $(r_n/r)_e \equiv -(d\, \ell n\, n_e/dr)^{-1}/r = 0.95$, and $\beta = 3.9\%$. Using a model equilibrium [10,11] with these values, the calculations yield the results plotted on Figs. 2-8. All frequencies are normalized to the local electron diamagnetic drift frequency ω_{*_e} in Figs. 2-5.

Growth rates (γ) as a function of β are given on Fig. 2 and the corresponding real frequencies (ω_r) are displayed on Fig. 3. For fixed density and temperature, the variation in β here simply corresponds to different input values for the toroidal magnetic field. To illustrate their relative magnitude, the value of the average ion transit frequency ($\bar{\omega}_{ti}$) along with $\bar{\omega}_{bi}$ and ν_{eff}^e are also indicated on Fig. 2. Curve (a) on this figure represents the ideal MHD estimate of the eigenvalues obtained from the familiar second order differential ballooning mode equation ignoring compressional acoustic effects. The real frequency in this limit is just $\omega_r = 0$. The curve here displays the usual trend indicating stability below an initial critical beta value ($\beta_{c1} = 1.1\%$) and also above an upper critical beta ($\beta_{c2} = 6.3\%$) with instability in the range $\beta_{c1} < \beta < \beta_{c2}$ [20,11]. As shown on curve (b) the introduction of both stabilizing and destabilizing kinetic

effects in the partial kinetic analysis (described in Sec. 2.3) leads to a moderate reduction of γ and no appreciable shift in the critical beta values [5]. However, as demonstrated in Sec. 2.1, the compressional acoustic dynamics ignored here can significantly further reduce the growth rates even in the ideal MHD limit. These effects together with the proper integral equation nature of the basic problem are taken into account in the full kinetic treatment described in Sec. 2.2. Results from these calculations in the collisionless limit are displayed as curve (c) representing the kinetic ballooning modes associated with shear Alfvén waves and curve (d) representing the trapped-electron modes associated with drift waves. Curve (c) indicates that the additional physical effects just discussed can indeed lead to a substantial reduction in the strength of the ballooning modes and to a moderate shift in the critical beta values. As shown on curve (d), the trapped-electron modes are unstable in the electrostatic limit ($\beta = 0$) and eventually become stabilized by electromagnetic modifications [21] at sufficiently high values of beta (e.g., at $\beta \simeq 2\%$ for this case).

The basic trend indicated by curves (c) and (d) of Fig. 2 is that short wavelength toroidal instabilities are likely to be present over a wide range in β with the drift branch dominant at low β and the Alfvén branch dominant at high β (i.e., for $\beta > \beta_{c1}$). However, at moderate values of β, both classes of instabilities can be significant. For example, at $\beta \simeq 1.3\%$, Fig. 2 indicates that the trapped-electron mode and the ballooning mode can be simultaneously present with comparable growth rates. Note that curves (c) and (d) of Fig. 3 verify that the corresponding real frequencies are, as expected, distinctively different. Also shown on this figure as curve (b) are the values of ω_r obtained from the partial kinetic code. Here $\omega_r \sim \omega_{*pi}/2$ in the unstable range of β with $\omega_{*pi} \equiv \omega_{*i}(1 + \eta_i)$. Although this is in reasonable agreement

with rough analytic estimates of the real frequency for unstable kinetic ballooning modes [1-4], the additional effects, which are included in the full kinetic analysis generating curve (c), tend to decrease substantially $|\omega_r|$ below $|\omega_{*pi}/2|$.

As discussed in Sec. 2.2, a model Krook operator is used to introduce collisional dissipation into the comprehensive calculations which produced curves (c) and (d). The resultant eigenvalues are displayed as curve (e) on Figs. 2 and 3. Here a single curve is used to represent the combined collisionally modified contributions from the two distinct types of modes represented by curves (c) and (d). This is done because collisions are found to damp out quickly the subdominant class of instabilities, thereby leaving only one significant branch for a given value of beta. To illustrate this trend, growth rates were calculated as a function of the collisionality parameter ν_e^* for the case with $\beta = 1.3\%$. As shown on Fig. 4, the results indicate that despite the fact that the growth rates are roughly of comparable magnitude in the collisionless limit, the ballooning branch is very rapidly damped by collisions while the drift branch remains unstable. At higher values of beta, the ballooning modes become dominant while the drift branch becomes damped. For the case displayed in Fig. 5 with $\beta = 3.9\%$, even the collisionless theory indicates only the ballooning branch to be relevant. Although the instabilities in this instance are too strong to be damped by collisions, their growth rates can nevertheless be significantly reduced. For example, at $\nu_e^* = 0.145$ (the collisionality noted earlier as being representative of ISX-B conditions of interest) both Fig. 5 and Fig. 2 [curves (c) and (e)] show the collisionally modified estimate to be roughly a factor of 3 below the collisionless growth rate. In general, this trend appears to be particularly pronounced in the ballooning-mode-dominated regimes and leads

to the qualitative picture [illustrated by curve (e) of Fig. 2] where the growth rate of the relevant instability changes in a continuous and quite gradual manner as a function of beta.

Comparison of the "hybrid" drift-ballooning curve (e) with the collisionless growth rates in Fig. 2 indicates that collisions tend to reduce uniformly the strength of the dominant modes over the usual accessible range of beta ($0 < \beta < \beta_{c2}$). However, at the high values of beta associated with the "second stability" regime ($\beta \gtrsim \beta_{c2}$), residual dissipative instabilities appear to persist up to larger beta values. With regard to the real frequency, Figs. 4 and 5 demonstrate that the collisional effects produce a shift of ω_r toward the electron diamagnetic direction. Accordingly, the collisional modifications of curves (c) and (d) in Fig. 3 lead effectively to the "hybrid" curve (e). As in the case of the growth rate curve, the curve for ω_r here also exhibits a relatively continuous and gradual dependence o beta.

The preceding analysis of eigenvalues indicates that neither making the ideal MHD approximation nor assuming the electrostatic limit can in general be justified when dealing with short-wavelength toroidal instabilities. This fact is further supported by results from the comprehensive kinetic studies of the eigenfunctions for these modes. As noted earlier, the ballooning representation is used in the calculations with the perturbed electrostatic potential expressed in the form

$$\Phi(\psi,\theta,\zeta,t) = \exp\,[-i\omega t + in\zeta - inq(\psi)\theta]$$

$$\times \sum_{p' = -\infty}^{\infty} \hat{\phi}(\theta - 2\pi p',\ \psi)\ \exp[inq(\psi)\ 2\pi p']. \qquad (6)$$

Note that Φ is periodic in the toroidal and poloidal angles, ζ and θ, while $\hat{\phi}(\theta)$ is defined in the infinite domain from $-\infty$ to ∞ in θ and is not periodic [10]. Similar forms apply for the perturbed parallel and perpendicular components of the magnetic vector potential, $A_\parallel$ and $A_\perp$, with $A_\perp$ taken here to be the radial component, i.e.,

$$A = A_\parallel \hat{n} + A_\perp \hat{e}_\psi \quad \text{where} \quad \hat{e}_\psi \equiv \nabla\psi/|\nabla\psi| \ .$$

Typical solutions for the eigenfunctions ($\hat{\phi}$, $\hat{A}_\parallel$, $\hat{A}_\perp$) obtained from the full kinetic collisionless analysis are illustrated on Figs. 6 and 7. The calculations, which have been applied here to the model equilibrium using ISX-B parameters with local $\beta = 1.3\%$, yield the eigenvalues, $\omega/\omega_{*_e} \approx -1.878 + 0.413i$ for the ballooning mode displayed on Fig. 6 and $\omega/\omega_{*_e} = -0.248 + 0.527i$ for the trapped-electron drift mode shown on Fig. 7. Also included in these figures is the eigenfunction for the effective parallel electric field,

$$\hat{E}_\parallel = -\frac{1}{qR_o}\frac{\partial\hat{\phi}}{\partial\theta} + \frac{i\omega}{c}\hat{A}_\parallel \qquad (7)$$

which is generally assumed to be zero in ideal MHD calculations. Validity of this approximation requires $|\hat{\psi}| \approx |\hat{\phi}| \gg |qR_o\hat{E}_\parallel|$ with $|\hat{\psi}| \equiv |\omega qR_o\hat{A}_\parallel/c|$. A comparison of the relative magnitudes of $|\hat{\phi}|$ and $|qR_o\hat{E}_\parallel|$ in Fig. 6 indicates that this condition is clearly not well satisfied at local positions in θ (e.g., near $\theta = \pm\pi$) for the ballooning mode studied. In order for the electrostatic limit to be appropriate, the requirement is that $|\hat{\phi}| \approx |qR_o\hat{E}_\parallel| \gg |\hat{\psi}|$. As shown on Fig. 7, the trapped-electron drift mode of interest obviously violates this criterion. Hence, these eigenfunction calculations serve to further emphasize that neither the familiar ideal MHD

assumption, $\hat{E}_{\parallel} = 0$, nor the electrostatic approximation, $\hat{E}_{\parallel} = -(1/qR_o)\ (d\hat{\phi}/d\theta)$ can be properly invoked in the analysis of short-wavelength instabilities in toroidal plasmas with moderate to high values of beta.

In previous studies [8] of trapped-electron drift instabilities it was reported that under relevant tokamak operating conditions a broad spectrum of unstable eigenvalues was usually found to occur. Results from the present analysis of ballooning modes also displays this characteristic. A typical spectrum of ballooning mode eigenvalues obtained from the full kinetic collisionless calculations applied to the model equilibrium ISX-B case with local $\beta = 3.9\%$ is shown on Fig. 8. The mode frequencies in units of 10^5 sec^{-1} are plotted here as a function of the toroidal mode number and the corresponding values of $k_\theta \rho_i$. Note that the growth rate varies rather slowly over a substantial range in n with the maximum occurring near $n = 10$ or $k_\theta \rho_i = 0.3$.

3.2 *PDX and DOUBLET-III*

Recent experimental results [22,23] have indicated that in neutral-beam-heated tokamaks with divertor geometry it is possible to produce so-called "H-mode" discharges characterized by confinement properties which are significantly improved over those of conventional ("L-mode") cases. In order to determine the short-wavelength stability properties associated with these conditions, the detailed analysis described in the preceding section has been applied to the PDX device during both its normal and improved confinement modes of operation [23]. The input parameters are chosen to be characteristic of a typical discharge at two different times; one before and one after the L-mode to H-mode transition [24]. This choice obviously allows for a more natural comparison of the results from the two cases.

For the PDX L-mode case, the specific local parameters at a representative magnetic surface (r/a = 0.66) are: $\varepsilon_o = 0.15$, $T_e = 0.543$ keV, $T_i = 0.875$ keV, $q = 1.41$, $r\, d\, \ell n\, q/dr = 0.91$, $n_e = 2.0 \times 10^{13}$ cm^{-3}, $\eta_e = 2.11$, $\eta_i = 2.56$, $n = 20$, $k_\theta \rho_i = 0.30$, $\nu_e^* = 0.22$, $(r_n/r)_e = 1.0$, and $\beta = 0.41\%$. The analytic model equilibrium [10,11] is again employed, and the same basic sequence of calculations described in Sec. 3.1 has been carried out.

As shown on Figs. 9-12, the results, aside from some differences in the detailed shapes of the curves, are qualitatively the same as those obtained for the ISX-B studies. Some quantitative differences in the eigenvalues are also observed. This is expected to occur because a number of the physical parameters for PDX (e.g., plasma size, local temperature gradients, etc.) can be significantly different from ISX-B values. In particular, note that the growth rate spectrum in Fig. 11 tends to peak at higher values of n than the ISX-B case shown on Fig. 8. This can be attributed in large part to the simple fact that the PDX plasma size is greater. Another example of expected quantitative variations is illustrated by the results for ω_r shown on Fig. 10 for the PDX case with $\eta_i = 2.6$ as compared to those shown on Fig. 3 for the ISX-B case with $\eta_i = 1.1$. The known tendency for the real frequency of kinetic toroidal instabilities to be shifted more strongly in the ion diamagnetic direction when η_i is larger [14] is clearly evident here.

In the PDX discharge considered, the plasma was experimentally observed to pass from the L-mode phase just analyzed into an improved confinement state. Parameters characteristic of this H-mode phase at the magnetic surface of interest (r/a = 0.66) are: $\varepsilon_o = 0.15$, $T_e = 0.78$ keV, $T_i = 1.05$ keV, $q = 1.27$, $r\, d\, \ell n\, q/dr = 0.71$, $n_e = 4.9 \times 10^{13}$ cm^{-3}, $\eta_e = 3.3$, $\eta_i = 3.7$, $n = 20$, $k_\theta \rho_i = 0.30$, $\nu_e^* = 0.24$, $(r_n/r)_e = 1.9$, and $\beta = 1.3\%$. These values together with the analytic model equilibrium [10,11] have been used in the same series

of stability calculations as the L-mode studies. The results depicted on Figs. 13-16 appear for the most part to be qualitatively similar to those from the ISX-B and PDX L-mode cases and again suggest that the basic trends described in Sec. 3.1 are quite general in character. A curious exception is that at high beta values the collisionless curve (c) of Fig. 13 indicates residual instability while the collisional curve (e) shows stability. With regard to quantitative differences, the most interesting one comes from a comparison of the maximum growth rate (in units of 10^5 sec^{-1}) for the H-mode spectrum shown in Fig. 15 versus the corresponding result from Fig. 11 for the L-mode case. The indication here is that the relevant instabilites tend to be weaker under H-mode conditions.

In order to determine more accurately the relative strength of the instabilites in the L-mode and H-mode cases, the comprehensive kinetic stability analysis has also been applied to realistic numerical equilibria. These equilibria were generated from standard MHD equilibrium codes [17] using experimentally determined radial profiles for the pressure and the safety factor q [24]. As noted earlier, the actual value of beta at the reference magnetic surface of interest is $\beta \approx 0.41\%$ for the L-mode case and $\beta \approx 1.3\%$ for the H-mode case. The corresponding representative eigenvalues obtained from the calculations are $\omega/\omega_{*_e} \approx -0.473 + 0.816$ for the L-mode and $\omega/\omega_{*_e} = -0.667 + 0.646i$ for the H-mode. However, since the equilibrium density gradients tend to be considerably weaker during the H-mode phase of such experiments [22,23], the conventional normalization of ω in terms of ω_{*_e} can be somewhat misleading when comparing eigenvalues. The appropriate choice is to express these results in actual physical units, i.e., $\omega(10^5\ sec^{-1}) \approx -0.703 + 1.212\ i$ for the L-mode and $\omega(10^5\ sec^{-1}) = -0.680 + 0.659i$ for the H-mode. As in the case of the model equilibrium, the instabilities under L-mode conditions

appear to be significantly stronger. This again is an expected quantitative trend because the basic destabilizing forces (associated with the pressure gradient in general and the density gradient in particular) are typically weaker for the H-mode. For the particular example cited here, the growth rate under realistic conditions is about 50% smaller for the H-mode case. This result is at least consistent with the experimentally observed improvement in the anomalous energy confinement time in that the strength of the relevant instabilities is found to be reduced significantly.

As already noted, short-wavelength toroidal instabilities under various realistic operating conditions tend to exhibit qualitatively similar properties. This is further supported by results from the application of comprehensive stability calculations to a case of interest [25] for the Doublet-III device [26]. At a representative magnetic surface ($r/a = 0.71$), the specific input parameters [25] are: $\varepsilon_o = 0.16$, $T_e = 0.36$ keV, $T_i = 0.37$ keV, $q = 1.14$, $r\, d\ln q/dr = 0.40$, $n_e = 3.4 \times 10^{13}$ cm^{-3}, $\eta_e = 0.93$, $\eta_i = 0.87$, $n = 20$, $k_\theta \rho_i = 0.28$, $\nu_e^* = 0.63$, $(r_n/r)_e = 0.43$, and $\beta = 2.64\%$. The corresponding results for the eigenvalues are shown on Figs. 17-19 and display the same general trends as the ISX-B and PDX cases.

4. CONCLUSIONS

In this paper a comprehensive kinetic analysis of the stability properties of short-wavelength modes under realistic tokamak operating conditions has been presented. These fully electromagnetic toroidal calculations deal with the kinetically generalized form of MHD ballooning modes together with the finite-β generalized form of the trapped-particle drift modes. Although the detailed results with comments about their implications have been given in Sec. 3, it is useful here to summarize briefly some of the principal conclusions.

With regard to properly calculating eigenvalues for unstable ballooning modes, it is demonstrated that even in the ideal MHD limit it is necessary to retain the terms associated with compressional ion acoustic waves. When the appropriate kinetic effects are also taken into account in the analysis, the resultant growth rates are found to be significantly smaller than those obtained from the usual ideal MHD [10,11] and simplified kinetic model [5] estimates. Collisional dissipation leads to a further reduction in these values over a wide range of beta , but in many cases it can also generate residual dissipative instabilities in the high-beta second stability regime. However, the accuracy of the Krook operator used to model collisions in these electromagnetic calculations remains to be established.

In general, the results from these studies indicate that for relevant experimental situations in tokamaks, short-wavelength instabilities with substantial growth rates should be excited over a broad spectrum of toroidal mode numbers. The trapped-electron drift modes are the most significant class of such instabilities at low β ($0 < \beta < \beta_{c1}$) while the kinetic ballooning modes appear to be the strongest type at higher β ($\beta > \beta_{c1}$). Although the strength of the dominant instability increases as beta increases from zero to values above β_{c1} and then decreases as β_{c2} is approached, the transitions in magnitude are relatively gradual. If one adopts the commonly accepted proposition that short-wavelength instabilites are primarily responsible for the observed anomalous transport in tokamaks, then the results here would support a "soft" beta limit picture for the impact of ballooning modes on confinement. As indicated by the relative strength of the dominant modes, it appears likely that as beta is increased, a continuous rather than an abrupt or "hard" modification of the anomalous transport already present at low beta would be observed. On the other hand, it should also be emphasized that the

increasing dominance of the electromagnetic component of the perturbations at higher beta could also lead to significantly different transport scaling properties from those associated with low beta (predominantly electrostatic) cases.

ACKNOWLEDGMENTS

The authors are grateful to Dr. J. K. Munro and Dr. D. J. Sigmar of Oak Ridge National Laboratory for providing the ISX-B numerical MHD equilibrium and radial profile data, to Dr. M. Kaye of Princeton University Plasma Physics Laboratory for providing the PDX radial profile data, and to Dr. R. Moore of GA Technologies for providing the Doublet-III numerical MHD equilibrium and radial profile data.

This work was supported by the United States Department of Energy, Contract NO. DE-AC02-76-CHO-3073.

REFERENCES

[1] TANG, W.M. CONNOR, J.W., HASTIE, R.J., Nucl. Fusion 20 (1980) 1439.

[2] TANG, W.M., CONNOR, J.W., WHITE, R.B., Nucl. Fusion 21 (1981) 891.

[3] HASTIE, R.J., HESKETH, K.W., Nucl. Fusion 21 (1981) 651.

[4] CHENG, C.Z., Phys. Fluids, 25 (1982) 1020.

[5] CHENG, C.Z., Nucl. Fusion 22 (1982) 773.

[6] COOPER, W.A., Plasma Phys. 24 (1982) 265.

[7] TANG, W.M., DEWAR, R.L., MANICKAM, J., Nucl. Fusion 22 (1982) 1079

[8] REWOLDT, G., TANG, W.M., CHANCE, M.S., Phys. Fluids 25 (1982) 480.

[9] CHANCE, M.S., DEWAR, R.L., FRIEMAN, E.A., GLASSER, A.H., GREENE, J.M., GRIMM, R.C., JARDIN, S.C., JOHNSON, J.L., MANICKAM, J., OKABAYASHI, M., TODD, A.M.M., in Plasma Physics and Controlled Nuclear Fusion Research (Proc 7th Int. Conf. Innsbruck, 1978) Vol. 1, IAEA, Vienna (1979) 677.

[10] CONNOR, J.W., HASTIE, R.J., TAYLOR, J.B., Phys. Rev. Lett. 40 (1978)396.

[11] LORTZ, D. NÜHRENBERG, J., Phys. Lett. 68A (1978) 49.

[12] DELUCIA, J., REWOLDT, G., Princeton University Plasma Physics Laboratory Report PPPL-1769 (1981).

[13] FRIEMAN, E.A., REWOLDT, G., TANG, W.M., GLASSER, A.H., Phys. Fluids 23 (1980) 1750.

[14] REWOLDT, G., TANG, W.M., FRIEMAN, E.A., Phys. Fluids 23 (1980) 2011.

[15] REWOLDT, G., TANG, W.M., Phys. Fluids 26 (1983) 3619.

[16] TANG, W.M., REWOLDT, G., Bull. Am. Phys. Soc. 27 (1982) 1105.

[17] GRIMM, R.C. GREENE, J.M., JOHNSON, J.L., in Methods in Computational Physics, edited by J. Killeen (Academic, New York, 1976) Vol. 16, 253; DELUCIA, J., JARDIN, S.C., TODD, A.M.M., J. Comput. Phys. 37 (1980) 183.

[18] MURAKAMI, M., SWAIN, D.W., BATES, S.C., BUSH, C.E., CHARLTON, L.A., et al., in Plasma Physics and Controlled Nuclear Fusion Research (Proc. 8th Int. Conf. Brussels, 1980) Vol. 1, IAEA, Vienna (1981) 377.

[19] MUNRO, J.K., SIGMAR, D.J. (private communication).

[20] COPPI, B., FERREIRA, A., MARK, J.W.K., RAMOS, J.J., Nucl. Fusion 19 (1979) 715.

[21] TANG, W.M., LIU, C.S., ROSENBLUTH, M.N., CATTO, P.J., CALLEN, J.D., Nucl. Fusion 16 (1976) 191; TANG, W.M., CHEN, L., RUTHERFORD, P.H., Bull. Am. Phys. Soc. 22 (1977) 1142.

[22] WAGNER, F., BECKER, G., BEHRINGER, K., CAMPBELL, D., EBERHAGEN, A., et al., Phys. Rev. Lett. 49 (1982) 1408; KEILHACKER, M., BECKER, G., BERNHARDI, K., EBERHAGEN, A., ELSHAER, M., et al., Plasma Phys. and Conf. Fusion 26, 1A (1984) 49.

[23] KAYE, S.M., GOLDSTON, R. J., BELL, M., BOL, K., BITTER, M., et al., Princeton University Plasma Physics Laboratory Report PPPL-2109 (1984).

[24] KAYE, S.M. (private communication)

[25] MOORE, R. (private communication)

[26] NAGAMI, M., and the JAERI Team, OVERSKEI, D., and the GA Team, in Plasma Physics and Controlled Nuclear Fusion Research (Proc. 9th Int. Conf. Baltimore, 1982) Vol. 1, IAEA, Vienna (1983) 27.

FIGURE CAPTIONS

FIG. 1 Ideal MHD ballooning mode growth rates ($-\Omega^2$) plotted as a function of radial position with ψ being the usual poloidal flux. Results from solutions to the second order and fourth order forms of the governing eigenmode equation are illustrated.

FIG. 2 Growth rates (γ) plotted as a function of β on a representative flux surface for a model equilibrium with ISX-B parameters. The curves represent: (a) the usual ideal MHD estimate for ballooning modes without coupling to compressional ion acoustic waves; (b) collisionless reduced kinetic model calculation in the same limit; (c) and (d) collisionless full kinetic results for the ballooning modes including acoustic coupling and the trapped-electron drift modes, respectively; and (e) a "hybrid" of (c) and (d) when collisional dissipation is modelled with a Krook operator. All frequencies are normalized to the electron diamagnetic drift frequency ω_{*e}.

FIG. 3. Real frequencies (ω_r) in units of ω_{*e} corresponding to the growth rate curves of Fig. 2. The real frequency for the ideal MHD curve (a) is just $\omega_r = 0$.

FIG. 4. Typical eigenvalues for trapped-electron drift modes and ballooning modes in units of ω_{*e} as a function of the collisionality parameter $\nu_e^* \equiv (\nu_{eff}/\bar{\omega}_b)_e$ for the full kinetic analysis applied to a model equilibrium using ISX-B parameters with local $\beta \approx 1.3\%$. Collisional effects are modelled in the full kinetic calculation here with a Krook operator.

FIG. 5. Typical ballooning mode eigenvalues plotted versus collisionality as in Fig. 4 but for the higher beta case where local $\beta = 3.9\%$.

FIG. 6. Typical eigenfunction calculated for the ballooning mode with the full kinetic collisionless analysis applied to a model equilibrium using ISX-B parameters with local $\beta = 1.3\%$. The poloidal angle, θ, here is the usual nonperiodic coordinate along the magnetic field line introduced by the ballooning representation.

FIG. 7. Typical eigenfunction calculated for the trapped-electron drift mode with the full kinetic collisionless analysis applied to the same case as Fig. 6.

FIG. 8. Typical spectrum of eigenvalues for ballooning modes with the full kinetic collisionless analysis applied to a model equilibrium using ISX-B parameters with local $\beta = 3.9\%$. Mode frequencies in units of 10^5 sec^{-1} are plotted as a function of the toroidal mode number (n) and the corresponding values of $k_\theta \rho_i$.

FIG. 9. Growth rates plotted as in Fig. 2 but for PDX L-mode parameters.

FIG. 10. Real frequencies corresponding to the growth rate curves of Fig. 9.

FIG. 11. Typical spectrum of eigenvalues plotted as in Fig. 8 but for PDX L-mode parameters with local $\beta = 2\%$ and $\nu_e^* = 0.22$.

FIG. 12. Typical ballooning mode eigenvalues plotted versus collisionality as in Fig. 4 but for PDX L-mode parameters with local β = 2%.

FIG. 13. Growth rates plotted as in Fig. 2 but for PDX H-mode parameters.

FIG. 14. Real frequencies corresponding to the growth rate curves of Fig. 13.

FIG. 15. Typical spectrum of eigenvalues plotted as in Fig. 8 but for PDX H-mode parameters with local β = 3% and ν_e^* = 0.24.

FIG. 16. Typical ballooning mode eigenvalues plotted versus collisionality as in Fig. 4 but for PDX H-mode parameters with local β = 3%.

FIG. 17. Growth rates plotted as in Fig. 2 but for Doublet-III parameters.

FIG. 18. Real frequencies corresponding to the growth rate curves of Fig. 17.

FIG. 19. Typical ballooning mode eigenvalues plotted versus collisionality as in Fig. 4 but for Doublet-III parameters with local β = 2.64%.

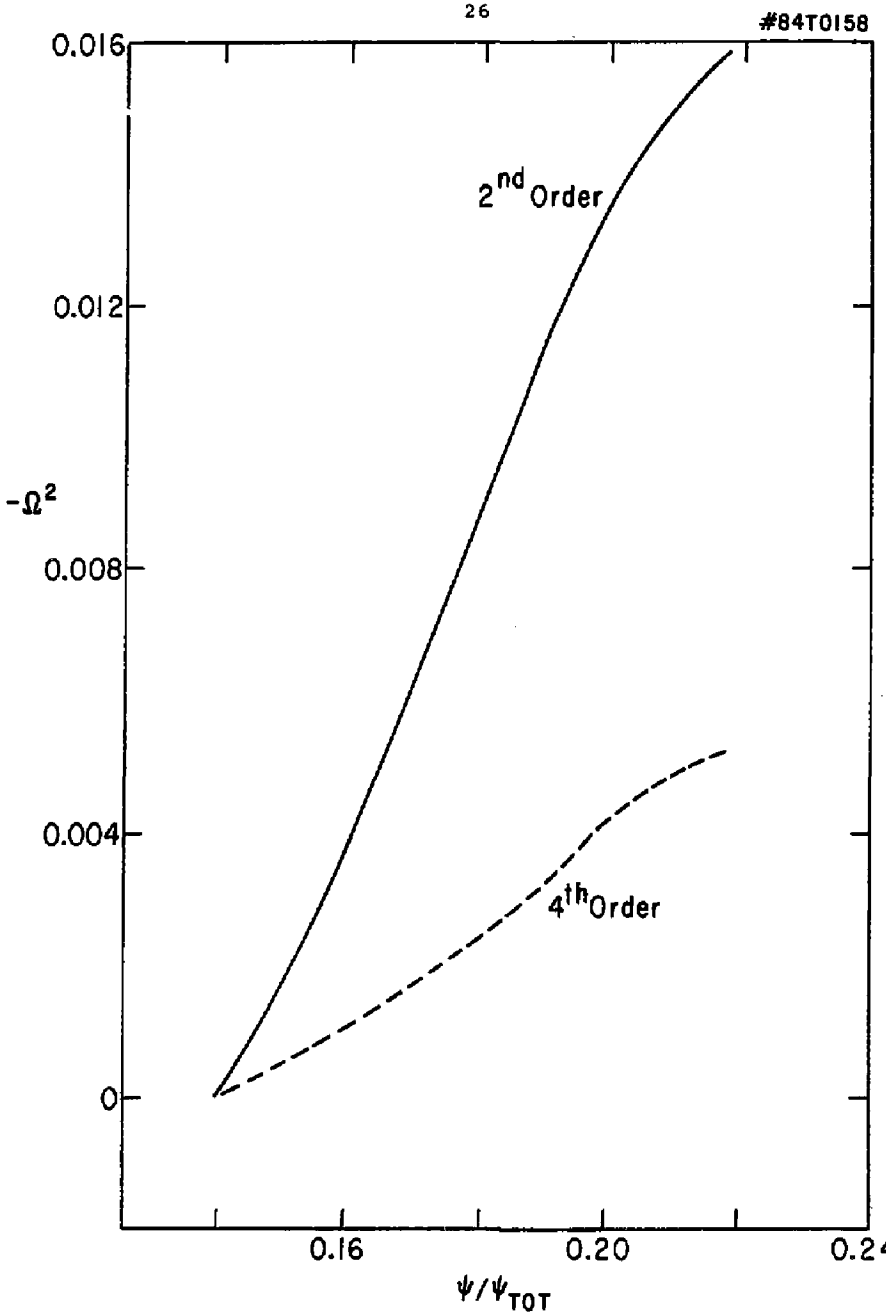
#84T0158
0.016
0.012
0.008
0.004
0
$-\Omega^2$
2nd Order
4th Order
0.16
0.20
0.24
ψ/ψ_{TOT}

Fig. 1

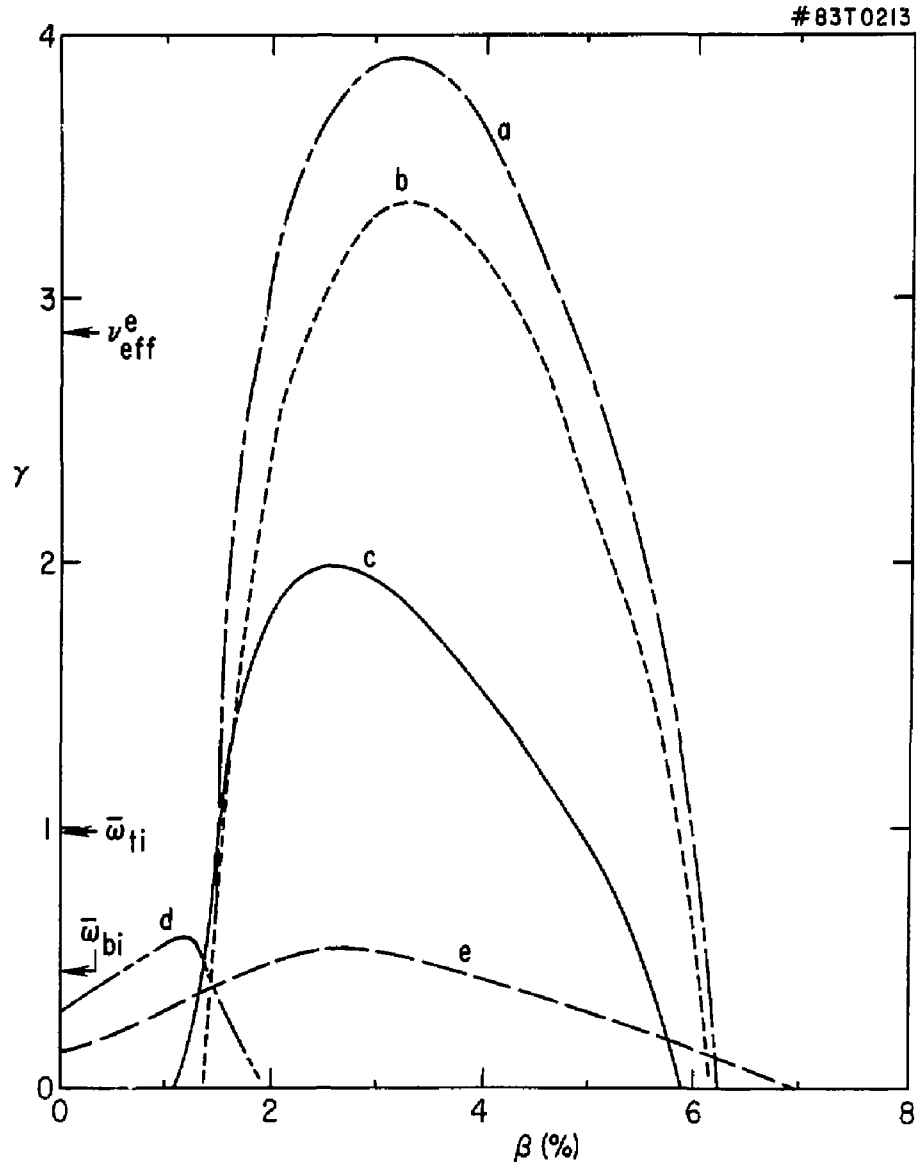
#83T0213
4
3
2
1
0
γ
ν^e_{eff}
$\bar{\omega}_{ti}$
$\bar{\omega}_{bi}$
a
b
c
d
e
0
2
4
6
8
β (%)

Fig. 2

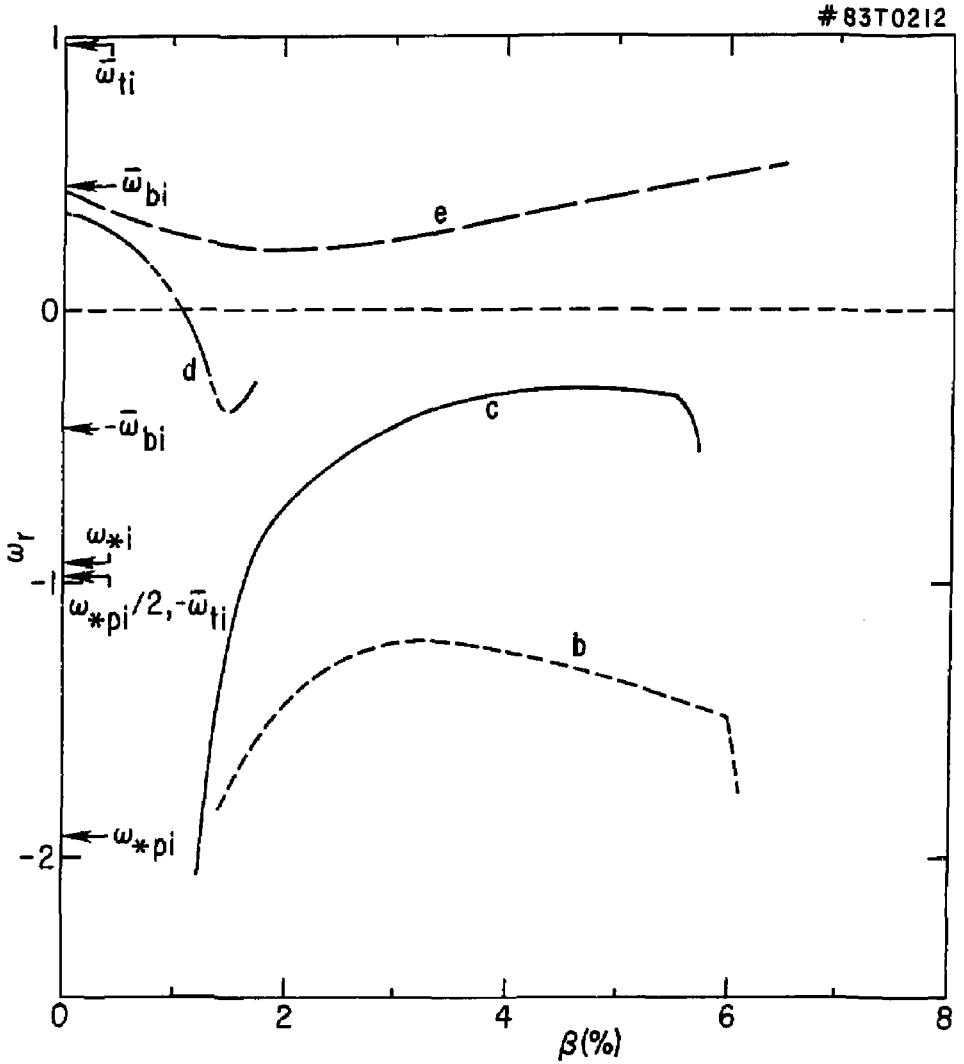
#83T0212
1
0
-1
-2
ω_r
$\bar{\omega}_{ti}$
$\bar{\omega}_{bi}$
$-\bar{\omega}_{bi}$
ω_{*i}
$\omega_{*pi}/2, -\bar{\omega}_{ti}$
ω_{*pi}
e
d
c
b
0
2
4
6
8
$\beta(\%)$

Fig. 3

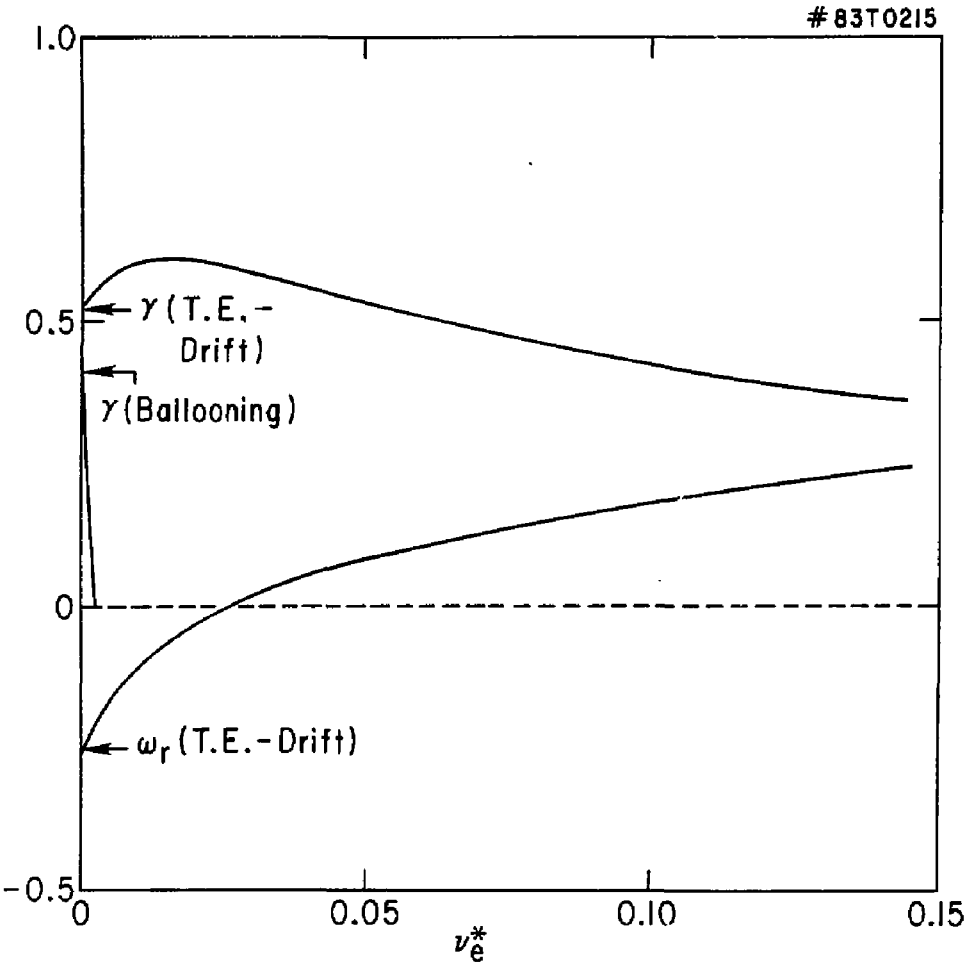
#83T0215
1.0
0.5
0
-0.5
0
0.05
0.10
0.15
ν_e^*
γ (T.E.- Drift)
γ (Ballooning)
ω_r (T.E.- Drift)

Fig. 4

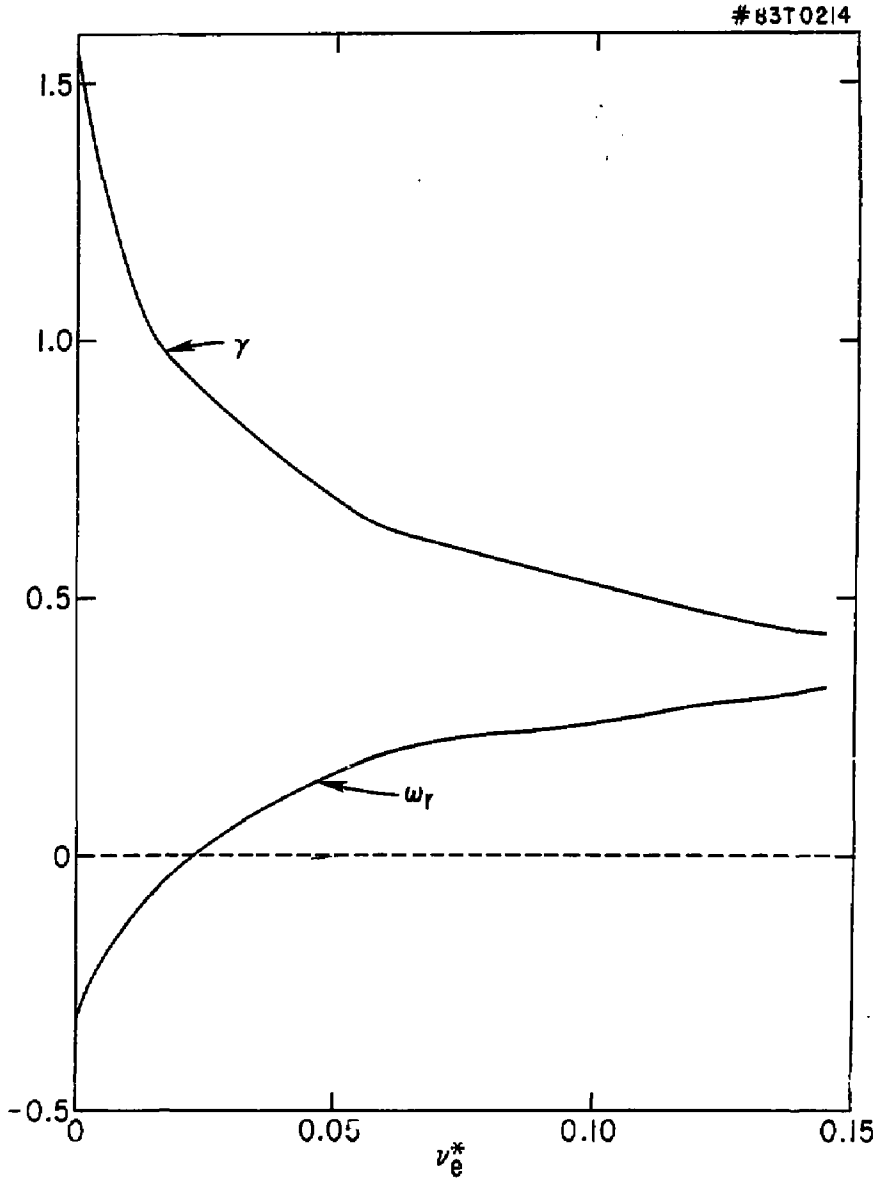

Fig. 5

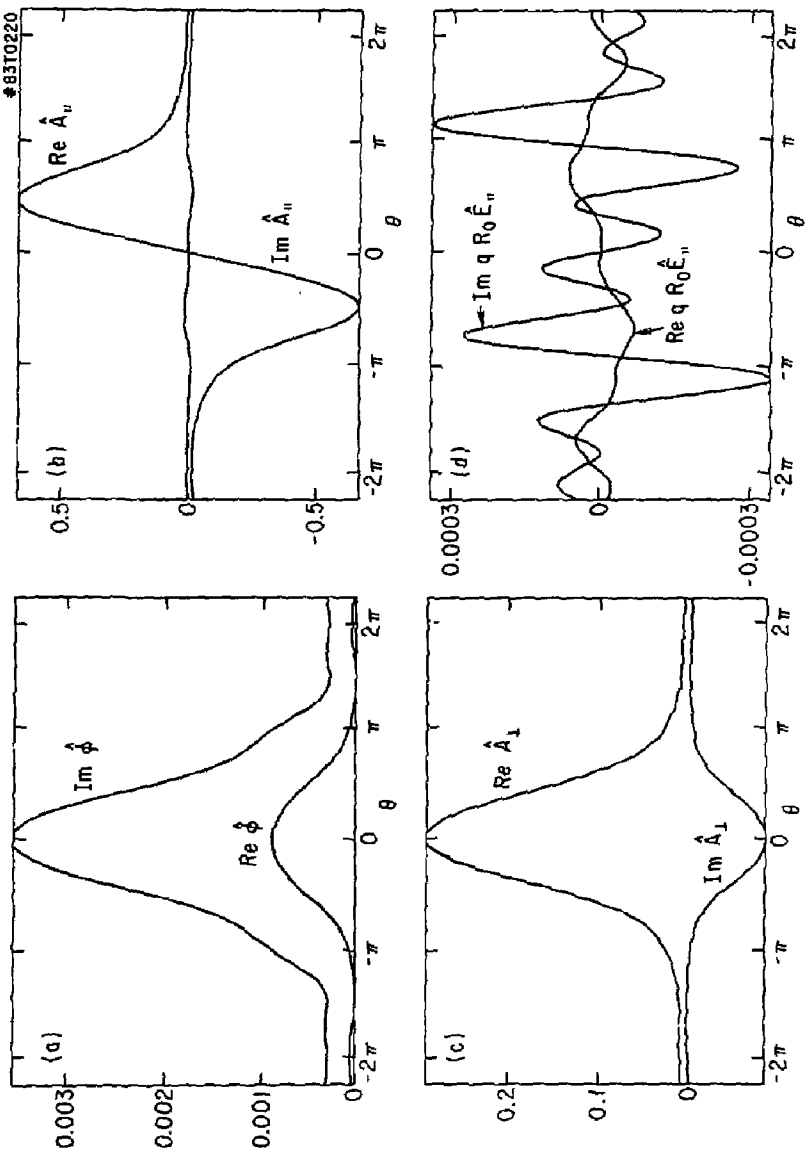
#83T0220
(a)
Im $\hat{\phi}$
Re $\hat{\phi}$
0.003
0.002
0.001
0
-2π
$-\pi$
0
π
2π
θ
(b)
Re $\hat{A}_u$
Im $\hat{A}_u$
0.5
0
-0.5
(c)
Re $\hat{A}_\perp$
Im $\hat{A}_\perp$
0.2
0.1
(d)
Im q $R_0\hat{E}_u$
Re q $R_0\hat{E}_u$
0.0003
-0.0003

Fig. 6

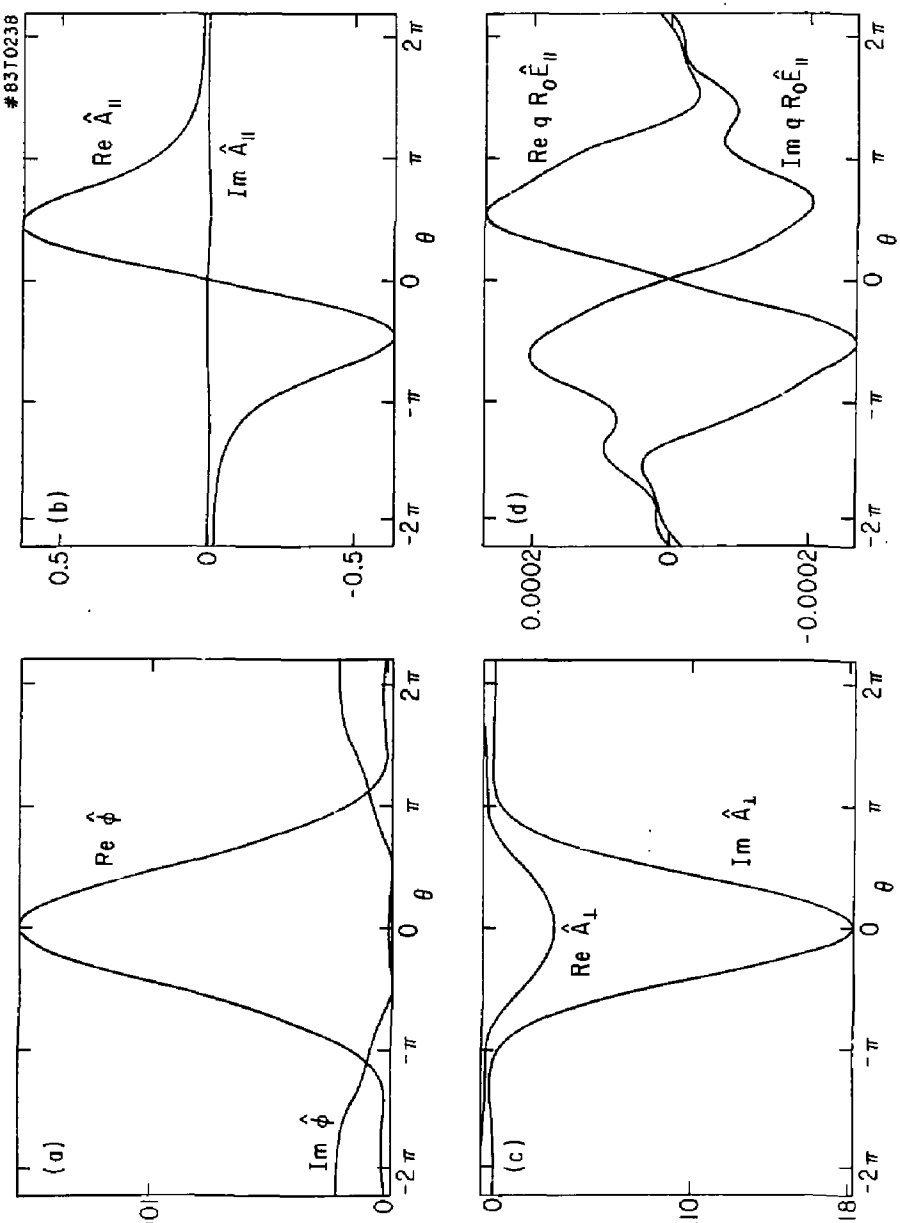
#8370238
(a)
Re $\hat{\phi}$
Im $\hat{\phi}$
0.001
0
(b)
Re $\hat{A}_{\parallel}$
Im $\hat{A}_{\parallel}$
0.5
0
-0.5
(c)
Re $\hat{A}_{\perp}$
Im $\hat{A}_{\perp}$
0
-0.10
-0.18
(d)
Re q $R_0\hat{E}_{\parallel}$
Im q $R_0\hat{E}_{\parallel}$
0.0002
0
-0.0002
-2π
$-\pi$
0
π
2π
θ

Fig. 7

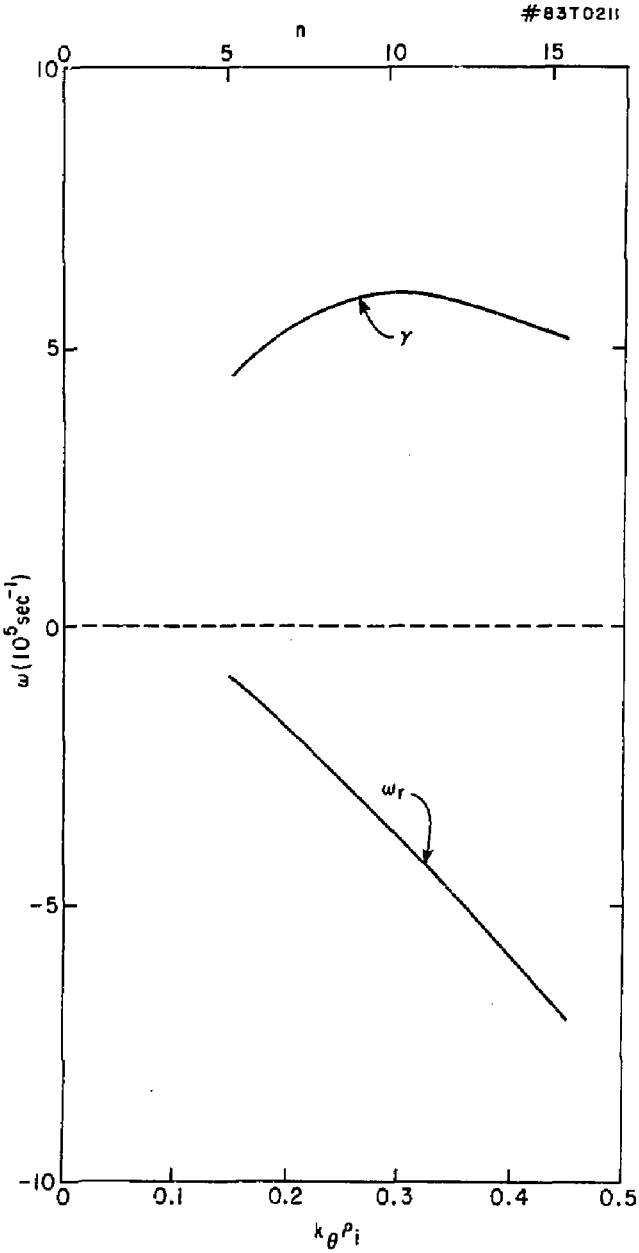
#83T0211
n
0
5
10
15
10
5
0
-5
-10
$\omega(10^5 sec^{-1})$
γ
ω_r
0
0.1
0.2
0.3
0.4
0.5
$k_\theta \rho_i$

Fig. 8

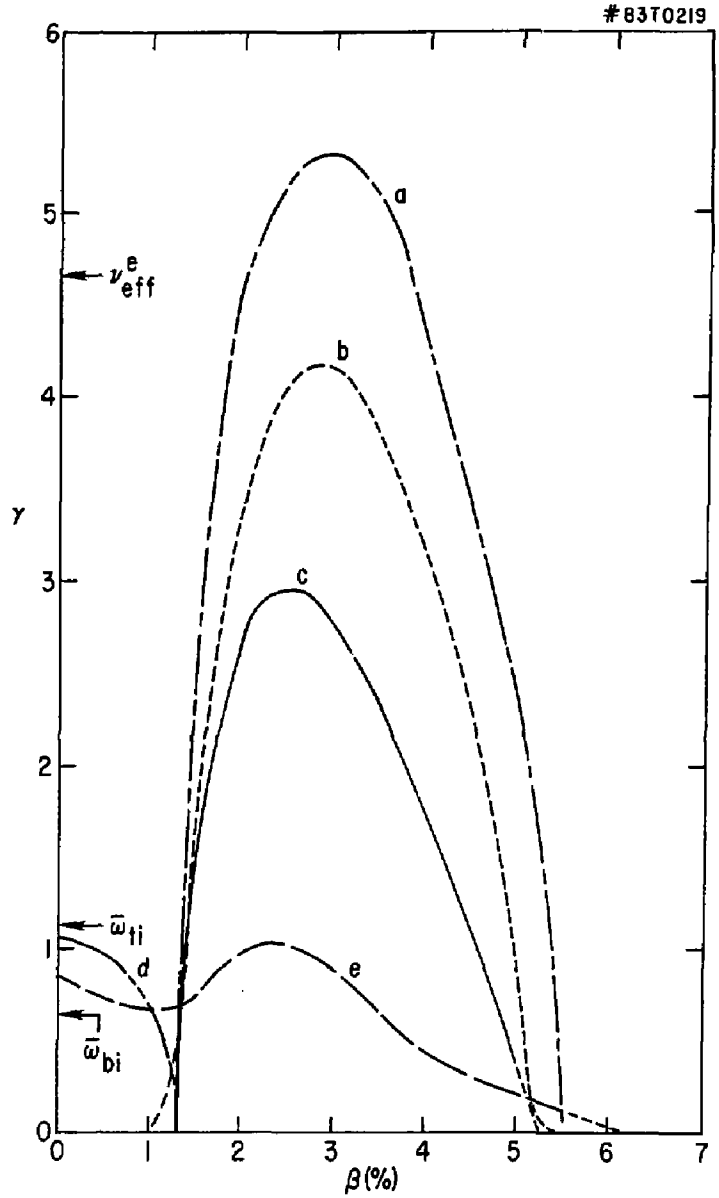
#83T0219
6
5
4
3
2
1
0
γ
ν^e_{eff}
a
b
c
d
e
$\bar{\omega}_{ti}$
$\bar{\omega}_{bi}$
0
1
2
3
4
5
6
7
β(%)

Fig. 9

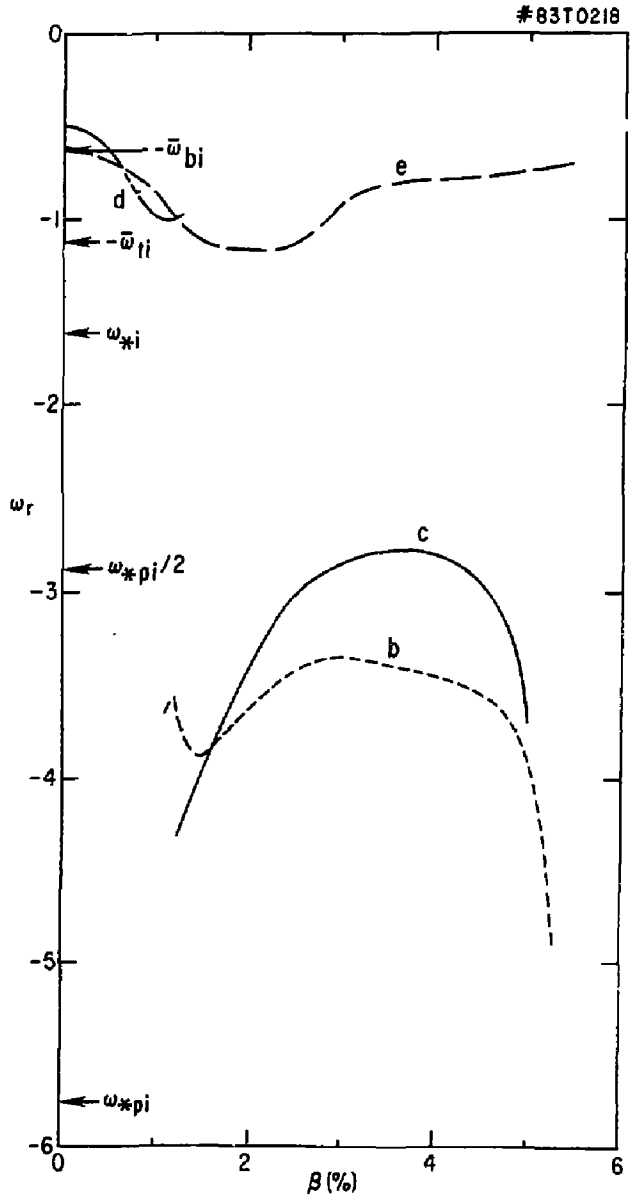
#83T0218
0
-1
-2
-3
-4
-5
-6
ω_r
$-\bar{\omega}_{bi}$
$-\bar{\omega}_{ti}$
ω_{*i}
$\omega_{*pi}/2$
ω_{*pi}
a
b
c
d
e
0
2
4
6
β(%)

Fig. 10

#83T0217

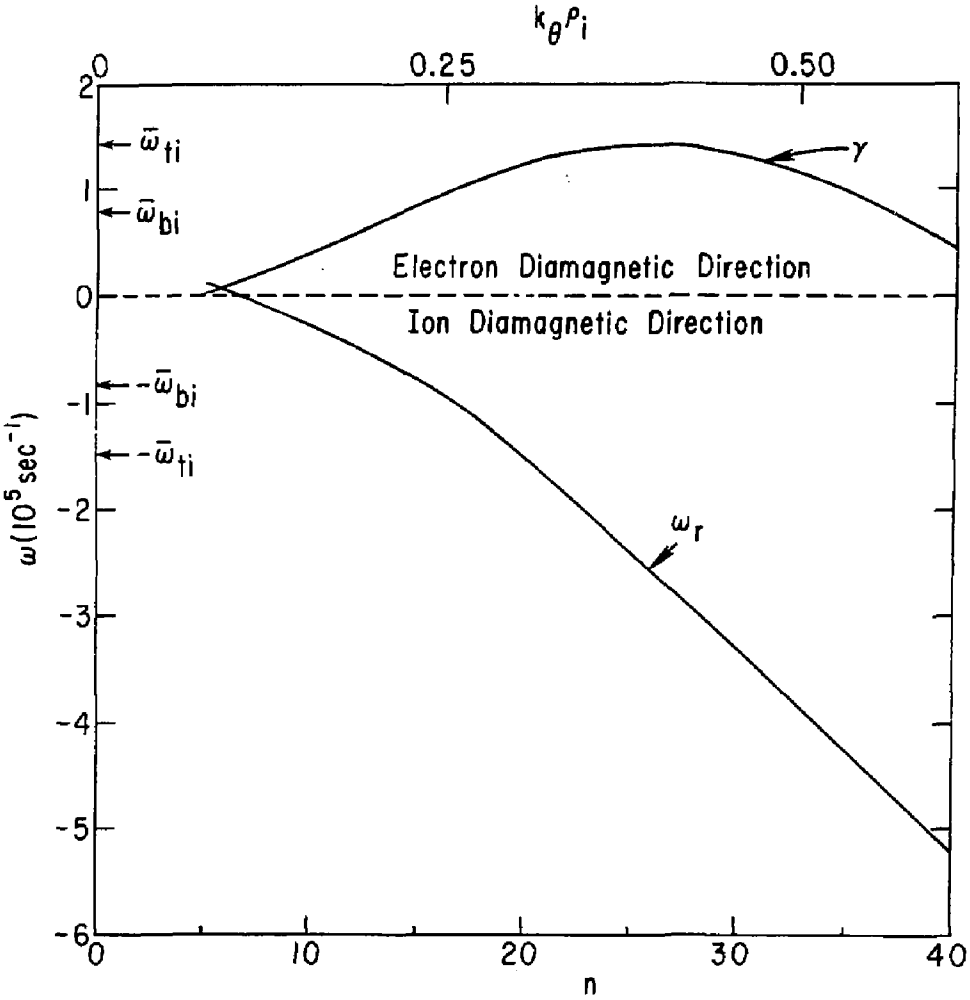

Fig. 11

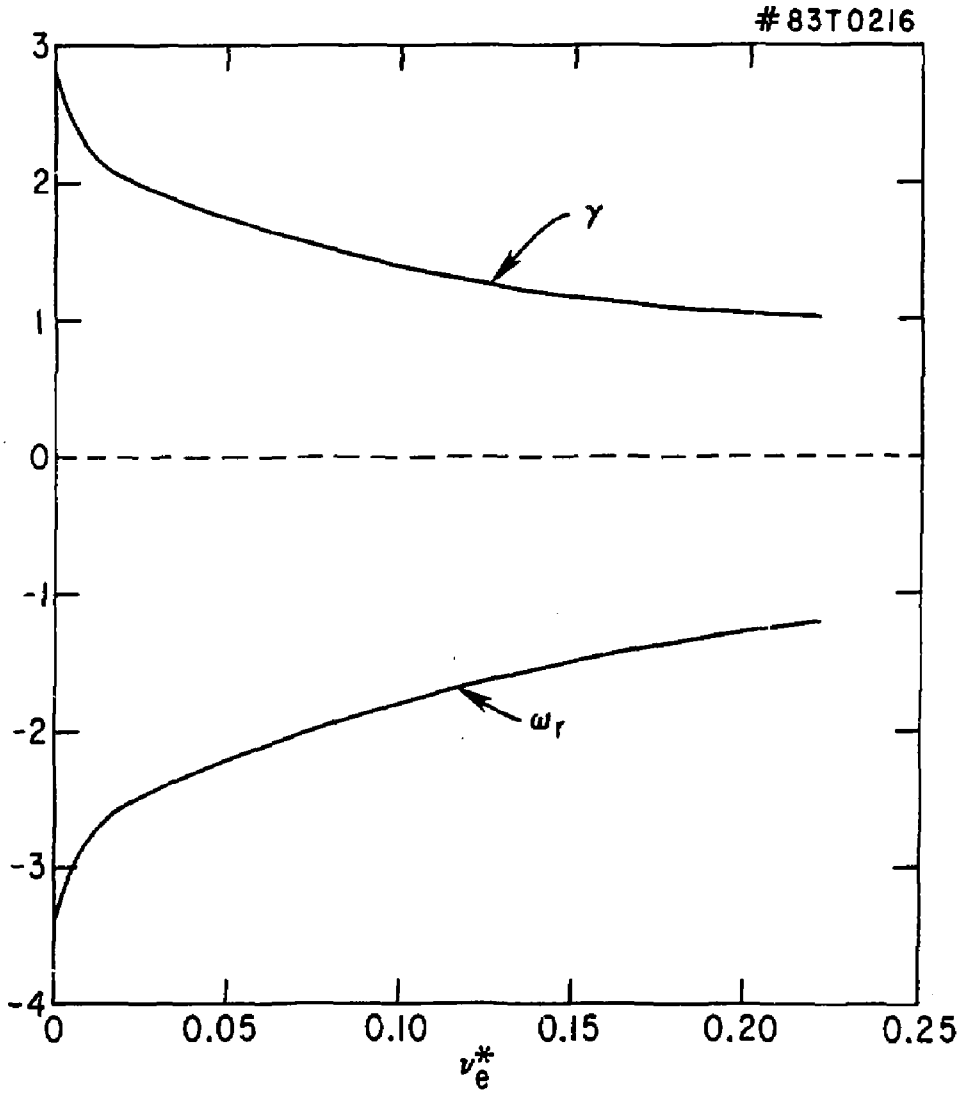

Fig. 12

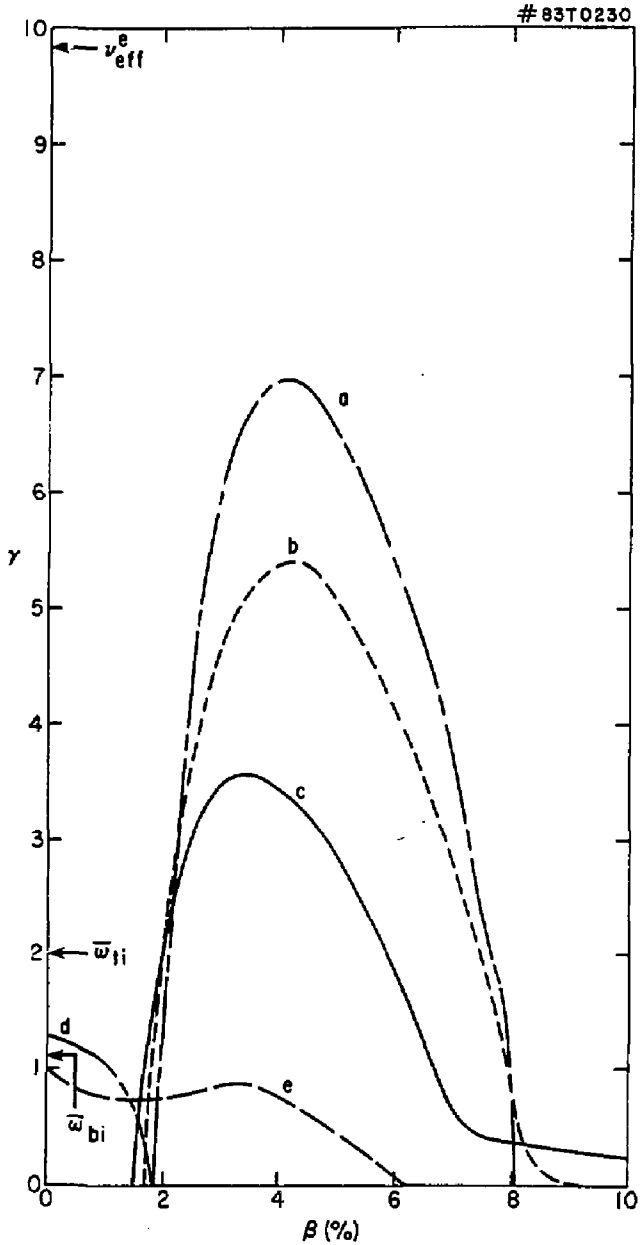
#83T0230
ν^e_{eff}
γ
a
b
c
d
e
$\bar{\omega}_{ti}$
$\bar{\omega}_{bi}$
β (%)
0
1
2
3
4
5
6
7
8
9
10

Fig. 13

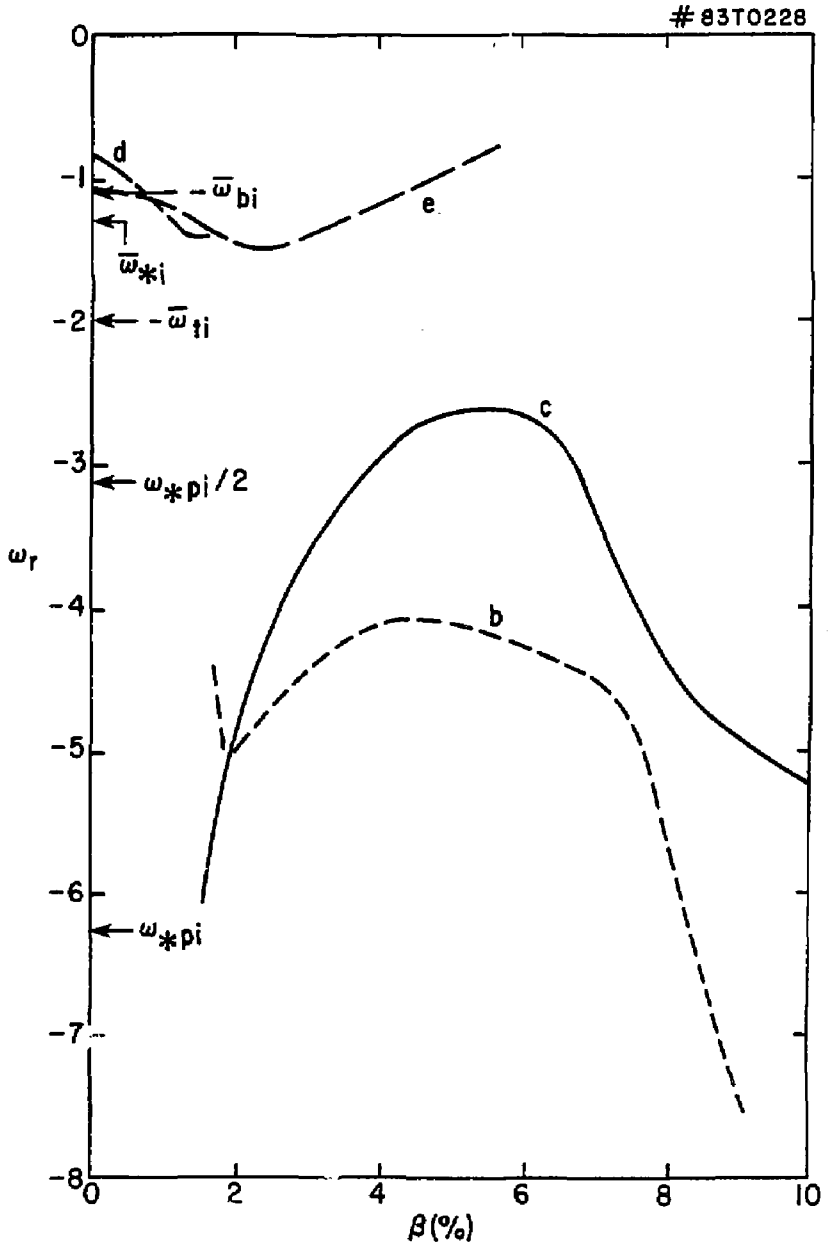
#83T0228
0
-1
-2
-3
-4
-5
-6
-7
-8
ω_r
d
$-\bar{\omega}_{bi}$
e
$\bar{\omega}_{*i}$
$-\bar{\omega}_{ti}$
c
$\omega_{*pi}/2$
b
ω_{*pi}
0
2
4
6
8
10
$\beta(\%)$

Fig. 14

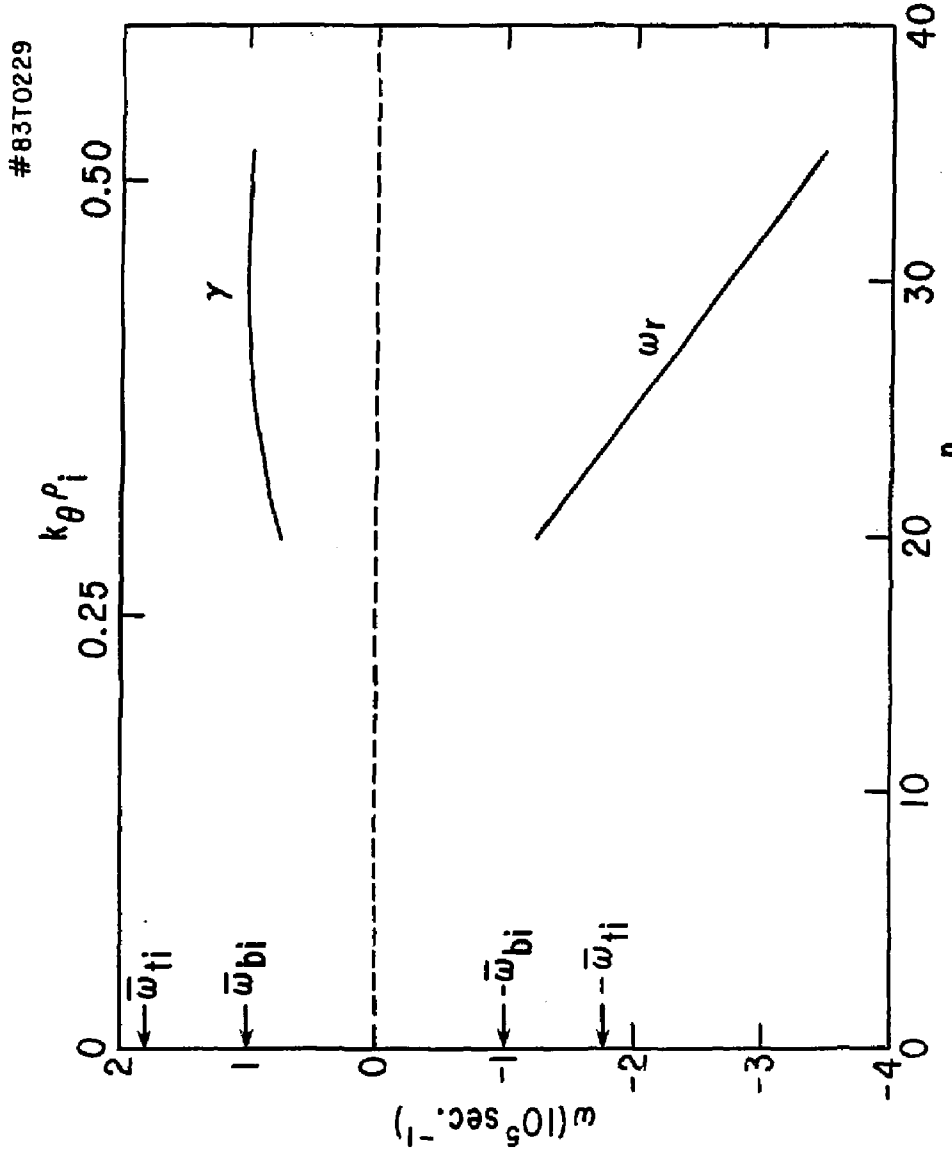
#83T0229
$k_\theta \rho_i$
0.25
0.50
γ
ω_r
$\bar{\omega}_{ti}$
$\bar{\omega}_{bi}$
$-\bar{\omega}_{bi}$
$-\bar{\omega}_{ti}$
$\omega(10^5 \text{sec.}^{-1})$
n
0
10
20
30
40
2
1
0
-1
-2
-3
-4

Fig. 15

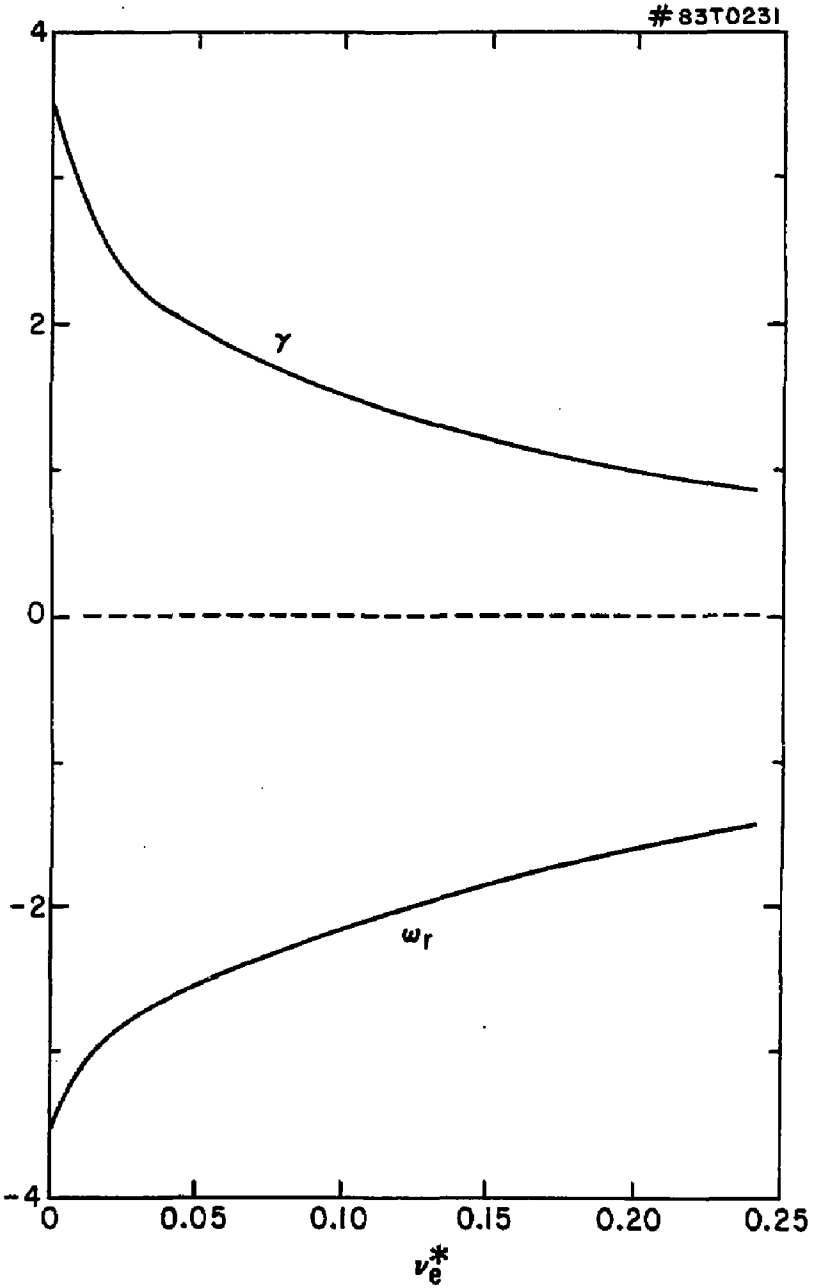

Fig. 16

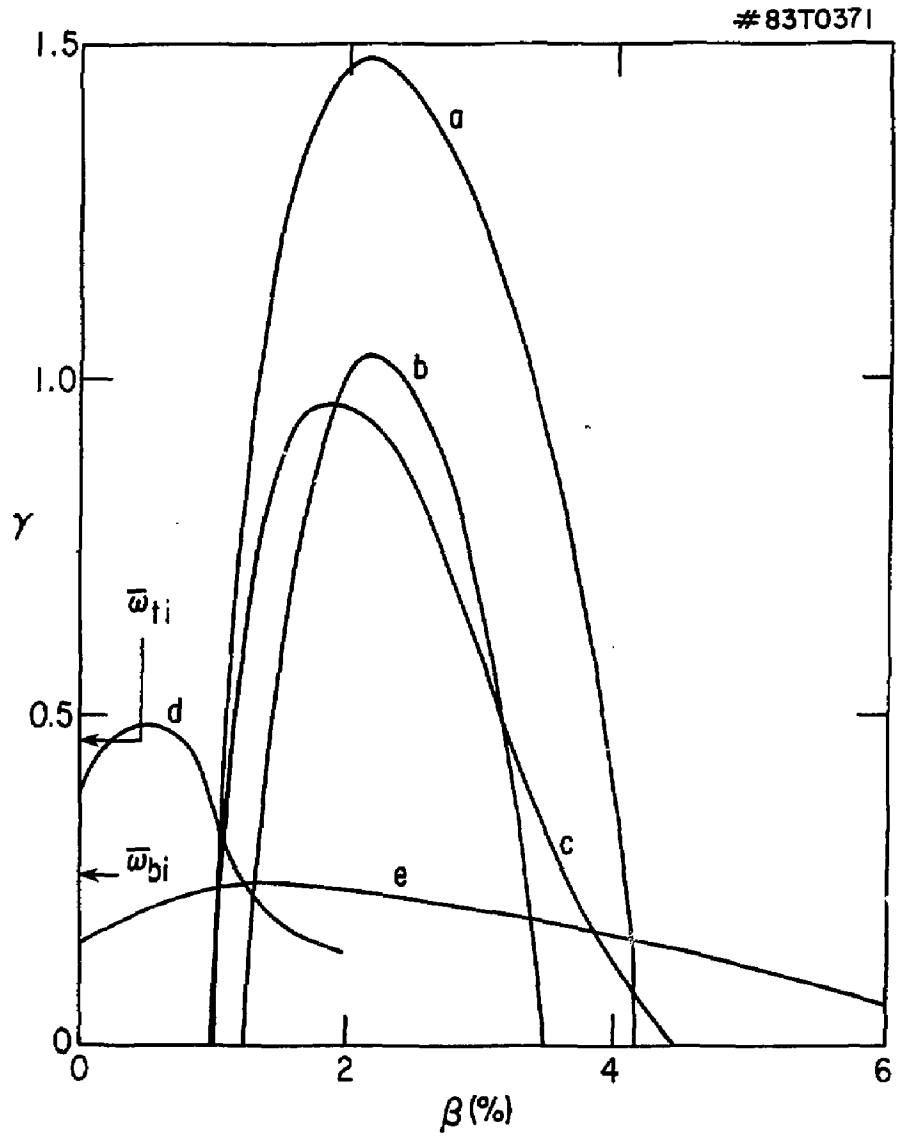

Fig. 17

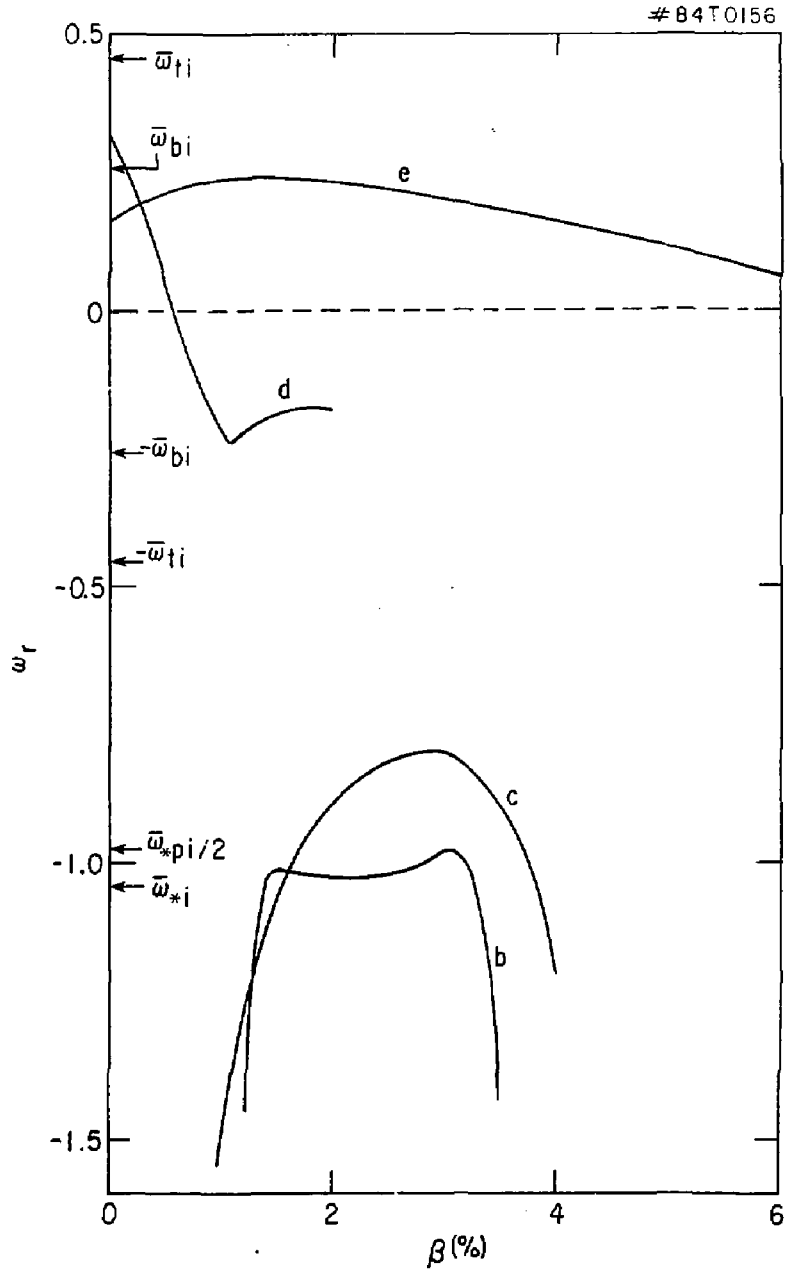
#84T0156
0.5
$\bar{\omega}_{ti}$
$\bar{\omega}_{bi}$
e
0
d
$-\bar{\omega}_{bi}$
$-\bar{\omega}_{ti}$
-0.5
ω_r
c
$\bar{\omega}_{*pi/2}$
-1.0
$\bar{\omega}_{*i}$
b
-1.5
0
2
4
6
β (%)

Fig. 18

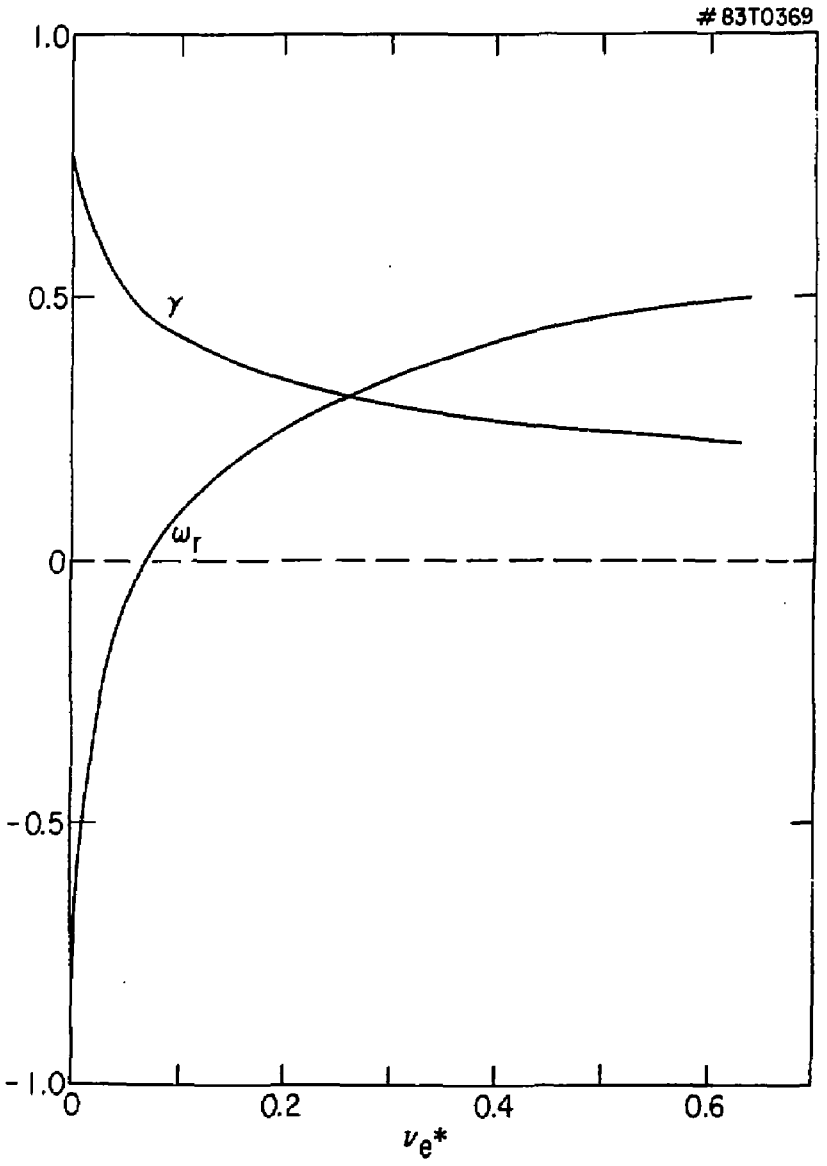

Fig. 19

EXTERNAL DISTRIBUTION IN ADDITION TO TIC UC-20

Plasma Res Lab, Austra Nat'l Univ, AUSTRALIA
Dr. Frank J. Paoloni, Univ of Wollongong, AUSTRALIA
Prof. I.R. Jones, Flinders Univ., AUSTRALIA
Prof. M.H. Brennan, Univ Sydney, AUSTRALIA
Prof. F. Cap, Inst Theo Phys, AUSTRIA
Prof. Frank Verheest, Inst Theoretische, BELGIUM
Dr. D. Palumbo, Dg XII Fusion Prog, BELGIUM
Ecole Royale Militaire, Lab de Phys Plasmas, BELGIUM
Dr. P.H. Sakanaka, Univ Estadual, BRAZIL
Dr. C.R. James, Univ of Alberta, CANADA
Prof. J. Teichmann, Univ of Montreal, CANADA
Dr. K.M. Skarsgard, Univ of Saskatchewan, CANADA
Prof. S.R. Sreenivasan, University of Calgary, CANADA
Prof. Tudor W. Johnston, INRS-Energie, CANADA
Dr. Hannes Barnard, Univ British Columbia, CANADA
Dr. M.P. Bachynski, MPB Technologies, Inc., CANADA
Zhengwu Li, SW Inst Physics, CHINA
Library, Tsing Hua University, CHINA
Librarian, Institute of Physics, CHINA
Inst Plasma Phys, Academia Sinica, CHINA
Dr. Peter Lukac, Komenskeho Univ, CZECHOSLOVAKIA
The Librarian, Culham Laboratory, ENGLAND
Prof. Schatzman, Observatoire de Nice, FRANCE
J. Radet, CEN-BP6, FRANCE
AM Dupas Library, AM Dupas Library, FRANCE
Dr. Tom Mual, Academy Bibliographic, HONG KONG
Preprint Library, Cent Res Inst Phys, HUNGARY
Dr. S.K. Trehan, Panjab University, INDIA
Dr. Indra, Mohan Lal Das, Benares Hindu Univ, INDIA
Dr. L.K. Chavda, South Gujarat Univ, INDIA
Dr. R.K. Chhajlani, Var Ruchi Marg, INDIA
P. Kaw, Physical Research Lab, INDIA
Dr. Phillip Rosenau, Israel Inst Tech, ISRAEL
Prof. S. Cuperman, Tel Aviv University, ISRAEL
Prof. G. Rostagni, Univ Di Padova, ITALY
Librarian, Int'l Ctr Theo Phys, ITALY
Miss Clelia De Palo, Assoc EURATOM-CNEN, ITALY
Biblioteca, del CNR EURATOM, ITALY
Dr. H. Yamato, Toshiba Res & Dev, JAPAN
Prof. M. Yoshikawa, JAERI, Tokai Res Est, JAPAN
Prof. T. Uchida, University of Tokyo, JAPAN
Research Info Center, Nagoya University, JAPAN
Prof. Kyoji Nishikawa, Univ of Hiroshima, JAPAN
Prof. Sigeru Mori, JAERI, JAPAN
Library, Kyoto University, JAPAN
Prof. Ichiro Kawakami, Nihon Univ, JAPAN
Prof. Satoshi Itoh, Kyushu University, JAPAN
Tech Info Division, Korea Atomic Energy, KOREA
Dr. R. England, Ciudad Universitaria, MEXICO
Bibliotheek, Fom-Inst Voor Plasma, NETHERLANDS
Prof. B.S. Liley, University of Waikato, NEW ZEALAND
Dr. Suresh C. Sharma, Univ of Calabar, NIGERIA
Prof. J.A.C. Cabral, Inst Superior Tech, PORTUGAL
Dr. Octavian Petrus, ALI CUZA University, ROMANIA
Prof. M.A. Hellberg, University of Natal, SO AFRICA
Dr. Johan de Villiers, Atomic Energy Bd, SO AFRICA
Fusion Div. Library, JEN, SPAIN
Prof. Hans Wilhelmson, Chalmers Univ Tech, SWEDEN
Dr. Lennart Stenflo, University of UMEA, SWEDEN
Library, Royal Inst Tech, SWEDEN
Dr. Erik T. Karlson, Uppsala Universitet, SWEDEN
Centre de Recherchesen, Ecole Polytech Fed, SWITZERLAND
Dr. W.L. Weise, Nat'l Bur Stand, USA
Dr. W.M. Stacey, Georg Inst Tech, USA
Dr. S.T. Wu, Univ Alabama, USA
Prof. Norman L. Oleson, Univ S Florida, USA
Dr. Benjamin Ma, Iowa State Univ, USA
Prof. Magne Kristiansen, Texas Tech Univ, USA
Dr. Raymond Askew, Auburn Univ, USA
Dr. V.T. Tolok, Kharkov Phys Tech Ins, USSR
Dr. D.D. Ryutov, Siberian Acad Sci, USSR
Dr. E.A. Ellseev, Kurchatov Institute, USSR
Dr. V.A. Glukhikh, Inst Electro-Physical, USSR
Institute Gen. Physics, USSR
Prof. T.J. Boyd, Univ College N Wales, WALES
Dr. K. Schindler, Ruhr Universitat, W. GERMANY
Nuclear Res Estab, Julich Ltd, W. GERMANY
Librarian, Max-Planck Institut, W. GERMANY
Dr. H.J. Kaeppler, University Stuttgart, W. GERMANY
Bibliothek, Inst Plasmaforschung, W. GERMANY